



HAL
open science

Physical Insights on the Lattice Softening Driven Mid-Temperature Range Thermoelectrics of Ti/Zr-Inserted SnTe-An Outlook Beyond the Horizons of Conventional Phonon Scattering and Excavation of Heikes' Equation for Estimating Carrier Properties

Ahmad Rifqi Muchtar, Bhuvanesh Srinivasan, Sylvain Le Tonquesse, Saurabh Singh, Nugroho Soelami, Brian Yulianto, David Berthebaud, Takao Mori

► To cite this version:

Ahmad Rifqi Muchtar, Bhuvanesh Srinivasan, Sylvain Le Tonquesse, Saurabh Singh, Nugroho Soelami, et al.. Physical Insights on the Lattice Softening Driven Mid-Temperature Range Thermoelectrics of Ti/Zr-Inserted SnTe-An Outlook Beyond the Horizons of Conventional Phonon Scattering and Excavation of Heikes' Equation for Estimating Carrier Properties. *Advanced Energy Materials*, 2021, 11 (28), pp.2101122. 10.1002/aenm.202101122 . hal-03357721

HAL Id: hal-03357721

<https://hal.science/hal-03357721>

Submitted on 29 Sep 2021

HAL is a multi-disciplinary open access archive for the deposit and dissemination of scientific research documents, whether they are published or not. The documents may come from teaching and research institutions in France or abroad, or from public or private research centers.

L'archive ouverte pluridisciplinaire **HAL**, est destinée au dépôt et à la diffusion de documents scientifiques de niveau recherche, publiés ou non, émanant des établissements d'enseignement et de recherche français ou étrangers, des laboratoires publics ou privés.

Physical Insights on the Lattice Softening Driven Mid-Temperature Range Thermoelectrics of Ti/Zr-Inserted SnTe—An Outlook Beyond the Horizons of Conventional Phonon Scattering and Excavation of Heikes' Equation for Estimating Carrier Properties

Ahmad Rifqi Muchtar, Bhuvanesh Srinivasan,* Sylvain Le Tonquesse, Saurabh Singh, Nugroho Soelami, Brian Yulianto, David Berthebaud,* and Takao Mori*

Most of the best known SnTe-based materials exhibit an attractive thermoelectric figure of merit (zT) only at the high-temperature regime, but their performance at the low-mid temperature ranges is quite uninspiring, and this discordance necessitates a large temperature gradient ($\Delta T \geq 550$ K) to effectuate a reasonable efficiency, η . Here, the transition elements, Ti and Zr, that have not been used in the past are tried as dopants for SnTe and an enhanced device/average zT and/or η are reported with a lower $\Delta T \approx 400$ K and without the requisite for a stupendous peak/maximum zT . This notable performance emanates from—i) improved weighted mobility by optimally balancing between effective mass, carrier concentration, and mobility, ii) coupling of charge carriers with magnetic entropy, and the paramount factor being the iii) weakening of the chemical bonds (lattice softening). The thermal damping caused by lattice softening affects the phonon group velocity and the elastic properties, and the resultant increase in the degree of anharmonicity and the high density of internal strain-fields, along with the phonon scattering effects, play an active role in tuning the overall thermoelectric performance. This work also excavates/opens up the discussion of applying the Heikes' equation to qualitatively compare the trend of charge carriers for a given thermoelectric material system.

1. Introduction

With their ability to directly convert heat into electricity without any moving parts and liquid components, thermoelectric devices can play a vital role in solving the global problem of energy and the environment.^[1–8] The heat source can come from the sun, the earth, and even the body heat. Another source is the waste heat that has been one of the world's problems, mainly from the inefficiency of human activities such as cooking, cooling or heating, industrial processing, and energy generation. A dimensionless figure of merit determines the efficacy of thermoelectric energy conversion, $zT = S^2\sigma T/\kappa$, where S , σ , T , and κ are the Seebeck coefficient, electrical conductivity, absolute temperature, and total thermal conductivity (sum of the electronic contribution, κ_e , and the lattice contribution, κ_{latt}), respectively. zT strongly hinges on a narrow domain/window of charge carrier densities. The intercoupling of other physical parameters presents a greater

A. R. Muchtar, Dr. B. Srinivasan, Prof. T. Mori
National Institute for Materials Science (NIMS)
WPI International Center for Materials Nanoarchitectonics
(WPI-MANA)
1-1 Namiki, Tsukuba 305-0044, Japan
E-mail: SRINIVASAN.Bhuvanesh@nims.go.jp;
MORI.Takao@nims.go.jp

 The ORCID identification number(s) for the author(s) of this article can be found under <https://doi.org/10.1002/aenm.202101122>.

© 2021 The Authors. Advanced Energy Materials published by Wiley-VCH GmbH. This is an open access article under the terms of the Creative Commons Attribution-NonCommercial-NoDerivs License, which permits use and distribution in any medium, provided the original work is properly cited, the use is non-commercial and no modifications or adaptations are made.

DOI: 10.1002/aenm.202101122

A. R. Muchtar, Prof. N. Soelami, Prof. B. Yulianto
Institute of Technology Bandung
Department of Engineering Physics
Research Center for Nanosciences and Nanotechnology
Bandung 40132, Indonesia
Dr. B. Srinivasan, Dr. S. L. Tonquesse, Dr. D. Berthebaud
CNRS-Saint Gobain-NIMS
IRL 3629
LINK
National Institute for Materials Science (NIMS)
1-1 Namiki, Tsukuba 305-0044, Japan
E-mail: David.BERTHEBAUD@cnrs.fr
Dr. S. Singh
Toyota Technological Institute
Research Center for Smart Energy Technology
Nagoya 468-8511, Japan

challenge in tuning this figure of merit, especially where it is essential to have both higher power factor ($PF = S^2\sigma$) and lower κ . The power factor is known to be boosted by manipulating the density of states near the Fermi energy, convergence of multiple band valleys, energy filtering effect, and so forth.^[9–18] The thermal conductivity is known to be suppressed by nano-structuring, rattling impurities, phonon mode softening, resonant bonding, and so forth.^[10,19–25]

The lead-free IV–VI chalcogenide semiconductor, SnTe with the same rock-salt crystal structure as PbTe and with better mechanical properties, is considered a viable eco-friendly option for thermoelectrics.^[26] However, the pristine SnTe has its drawbacks with regards to its usage as a thermoelectric material such as high charge carrier concentration ($\approx 10^{21} \text{ cm}^{-3}$) due to the intrinsic nature of SnTe to have high Sn vacancies, small bandgap often leading to bipolar conduction, and the large energy separation between the two valence band maxima ($\approx 0.35 \text{ eV}$), all of which leads to a low S and high κ_e , thus ultimately lower zT in pristine stoichiometric SnTe.^[26–31] Due to larger anharmonicity and effective phonon scattering, PbTe exhibits lower thermal conductivity than SnTe.^[32–35] Various attempts and strategies have been made in the past to improve the thermoelectric performance in SnTe, which includes self-compensation in the composition with some additional Sn content;^[36,37] electronic bandstructure engineering—fostering resonance state in the vicinity of Fermi-level (mostly induced by In as a dopant in SnTe),^[27,38] simultaneous increase of principal bandgap and convergence of the light hole and heavy hole valence bands (realized with dopants such as Cd, Hg, Mn, Mg, Ca, and few more),^[27,29,36,37,39–44] and this also includes valence band inversion or crossing effects; and a diverse nano-structuration approaches to engineer the dense interstitials, stacking faults, point defects, nano-precipitates and semi-coherent interfaces, dislocations, strain clusters, and so forth,^[45–52] (by alloying with Cu_2Te , CdS , SrTe , ZnS , and a few more).^[53] All these approaches and dopants in SnTe, though they yielded an improved thermoelectric performance ($zT_{\text{max}} > 1$), are limited for any practical applications, as their improved performance happened only at higher temperature ranges (usually between 823 and 873 K, or higher) for SnTe-based materials. In the mid-temperature ranges ($\leq 723 \text{ K}$), for most of those reported compounds, the zT_{max} hardly crossed 0.5. Because of this disparity in performance over the mid and high-temperature regions, the average zT (zT_{ave}) and/or the thermoelectric conversion efficiency of the reported SnTe-based materials are higher, only when the temperature gradient is larger, that is, only when ΔT or $T_h - T_c > 550 \text{ K}$, where T_c is the temperature at the cold junction (usually 300 K) and T_h is the temperature at the hot junction (usually above 850 K for SnTe).^[28,54] Moreover, at such high-temperature ranges, SnTe-based materials tend to get oxidized, thus raising the issue of stability and cycling reproducibility of the transport property values.

This work aims to explore some new dopants that have not been tried in the past for SnTe, especially the transition elements, and with an objective to find something that is thermoelectrically competitive at the mid-temperature ranges ($\leq 723 \text{ K}$). Motivated by the promising results of few transition metals like V as a dopant in SnTe,^[50] in this work, Ti and Zr are explored as potential dopants. Ti and Zr, with their high oxidation states,

are expected to optimize the carrier concentration in an otherwise vacancy-rich SnTe. In this work, the strategy was that, if any of the compositions from the newly tried Ti and Zr series showed promising transport properties, then those optimized compositions are finally codoped with Mn, which is widely reported to bring in band convergence effect in SnTe.^[29,41] In a nutshell, this work investigates the effect of doping the transition metals Ti and Zr and their best performing optimized codoping (Ti-Mn and Zr-Mn) on the structural, electronic, and thermoelectric properties of SnTe. More specifically, the discussion and comparison of thermoelectric transport properties of the SnTe-based materials that are presented here are kept within the realistic/practically applicable temperature ranges ($T_{\text{max}} \approx 723 \text{ K}$, and $\Delta T \approx 400 \text{ K}$), in contrary to the attractive yet practically limited thermoelectric performances reported at high-temperature ranges for several SnTe analogues. From a larger perspective, this work also strives to provide a deep understanding of the transport properties of these SnTe materials based on different physical transport models, besides validating some unique ideas or advances/models that are proposed recently,^[55–57] and additionally, reiterates some alternative methods and physical insights^[58] that are underutilized/missed by the thermoelectric scientific community.

2. Results and Discussion

2.1. Crystal Structure and Sample Purity of Ti and Zr-Doped SnTe Compounds

The powder XRD patterns of the Ti and Zr doped samples, $\text{Sn}_{1-x}\text{Ti}_x\text{Te}$ and $\text{Sn}_{1-x}\text{Zr}_x\text{Te}$ ($0 \leq x \leq 0.05$; x is nominal) are shown in **Figure 1**. The XRD patterns of these SPS processed samples can be well indexed to the NaCl-type face-centered cubic (fcc) SnTe phase ($Fm\bar{3}m$, space group $n^\circ 225$). Also observed is the minor proportion of metallic Sn phase ($I4/mmm$, space group $n^\circ 141$), as in agreement with the previous studies,^[59] is known to be segregated at the grain boundaries.^[60] Other secondary phases start to appear at higher content of Ti or Zr ($x \geq 0.05$).

The Le Bail fitted XRD patterns for $\text{Sn}_{0.97}\text{Ti}_{0.03}\text{Te}$ and $\text{Sn}_{0.98}\text{Zr}_{0.02}\text{Te}$ are shown in **Figure 2** and the evolution of the extracted lattice parameters for all the Ti and Zr-doped compositions are shown in **Figure 3**. In the case of the $\text{Sn}_{1-x}\text{Zr}_x\text{Te}$ series, the lattice constant (a) decreases linearly from $x = 0$ to 0.04 with a value of $6.3255(4) \text{ \AA}$ and $6.3160(5) \text{ \AA}$, respectively. Assuming Zr to be in its stable IV-oxidation state, such a trend is expected, as Zr^{4+} with a smaller ionic radius of 86 pm is substituting for Sn^{2+} that has a larger ionic radius of 93 pm, and it follows the solid-solution Vegard's law (up to $x \leq 0.04$). There is no change in the lattice parameter at higher Zr-content ($x = 0.05$), confirming that the solubility limit of Zr in SnTe is $x < 0.05$.

In the $\text{Sn}_{1-x}\text{Ti}_x\text{Te}$ series, all the compositions show a similar lattice parameter of about 6.325 \AA . This is surprising, considering the much smaller ionic radius of Ti^{4+} (74 pm) than Sn^{2+} (93 pm). The deviations from the expected trend might be attributed to some changes in the local structure around the atoms and/or some complex effects affecting the average bonding distance,^[61] any of which will be difficult to be detected by XRD. Similar to that of Zr-doping, the apparition of the secondary

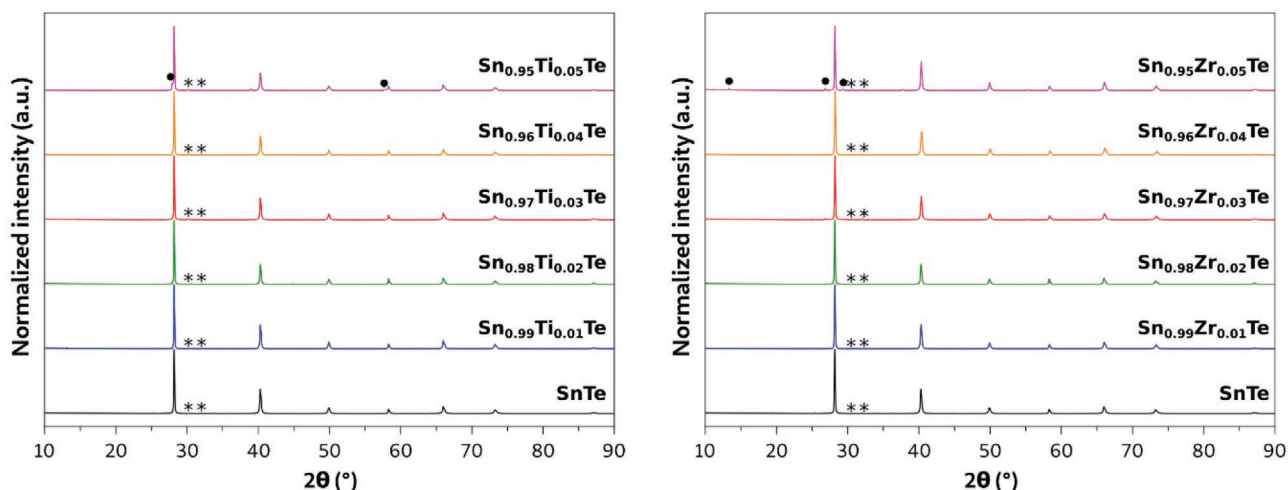


Figure 1. Room temperature powder XRD patterns of $\text{Sn}_{1-x}\text{Ti}_x\text{Te}$ (left) and $\text{Sn}_{1-x}\text{Zr}_x\text{Te}$ (right) samples ($0 \leq x \leq 0.05$). Asterisks indicate the elemental Sn phase and the black circles (at $x = 0.05$) indicate the appearance of other secondary phases.

phase at higher Ti-content confirms that the solubility limit of Ti in SnTe is crossed at $x = 0.05$. This solubility limit of $x \leq 0.04$ for Ti or Zr in SnTe is much higher when compared to dopants such as Co or Ni,^[62] and similar to that of dopants such as Ge,^[62] In,^[59] and lower compared to dopants such as Sb,^[63] Mn,^[27] Ca.^[37]

A representative SEM-EDX chemical/elemental mapping of the $\text{Sn}_{0.98}\text{Zr}_{0.02}\text{Te}$ sample presented in **Figure 4** reveals the compositional micro-homogeneity, particularly the dopant's uniform distribution in the SnTe material without any aggregation.

2.2. Transport Properties of Ti and Zr-Doped SnTe Compounds

The temperature-dependent electrical and thermal transport properties of Ti and Zr-doped SnTe compounds are presented in **Figures 5** and **6**, respectively. In both the cases ($\text{Sn}_{1-x}\text{M}_x\text{Te}$, with $M = \text{Ti}$ or Zr), the continuous decrease of electrical conductivity with temperature (**Figures 5a** and **6a**) suggests a degenerate semiconducting behavior, and the positive Seebeck coefficient (**Figures 5b** and **6b**) confirms the p-type charge transport in these systems, that is, holes as predominant charge

carriers. Barring some anomalies, Ti or Zr's doping to SnTe decreases the electrical conductivity and subsequently increases the Seebeck coefficient. The changes/differences in the electrical transport properties (σ and S) with dopant content are more pronounced in the case of Zr when compared to Ti. In particular, the changes in the electrical transport properties with the Zr-content are notable throughout the whole temperature range (323–723 K). In contrast, the changes are significant only at lower temperature ranges in the case of Ti-doping. The optimum balance between σ and S is achieved for the cases of $x = 0.03$ for Ti and $x = 0.02$ for Zr in these $\text{Sn}_{1-x}\text{M}_x\text{Te}$ ($M = \text{Ti}$ or Zr) compounds, as reflected in their power factor ($\text{PF} = S^2\sigma$) values, shown in **Figures 5c** and **6c**. It is important to note that the PF values for these optimized compositions of $\text{Sn}_{0.97}\text{Ti}_{0.03}\text{Te}$ and $\text{Sn}_{0.98}\text{Zr}_{0.02}\text{Te}$ are enhanced not only at a specific temperature, but rather enhanced throughout the whole temperature range. The improvement in PF values is quite significant even at low-temperature ranges. For instance, even at 323 K, the PF drastically increased (almost tripled) from $0.23 \times 10^{-3} \text{ W m}^{-1} \text{ K}^{-2}$ for pristine SnTe to $0.61 \times 10^{-3} \text{ W m}^{-1} \text{ K}^{-2}$ for $\text{Sn}_{0.97}\text{Ti}_{0.03}\text{Te}$ and to $0.68 \times 10^{-3} \text{ W m}^{-1} \text{ K}^{-2}$ for $\text{Sn}_{0.98}\text{Zr}_{0.02}\text{Te}$ compounds, and this superiority in PF is maintained right from room temperature

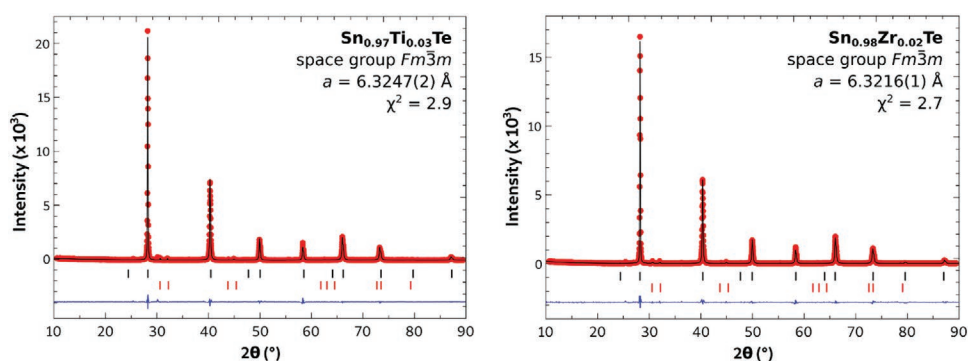


Figure 2. Le Bail refined room temperature XRD patterns of the best optimized $\text{Sn}_{0.97}\text{Ti}_{0.03}\text{Te}$ (left) and $\text{Sn}_{0.98}\text{Zr}_{0.02}\text{Te}$ (left) compounds. The experimental pattern is plotted with red symbols, the calculated pattern with black lines, and the difference with blue lines. The vertical ticks indicate the Bragg positions of the SnTe main phase (black) and the Sn impurity phase (red).

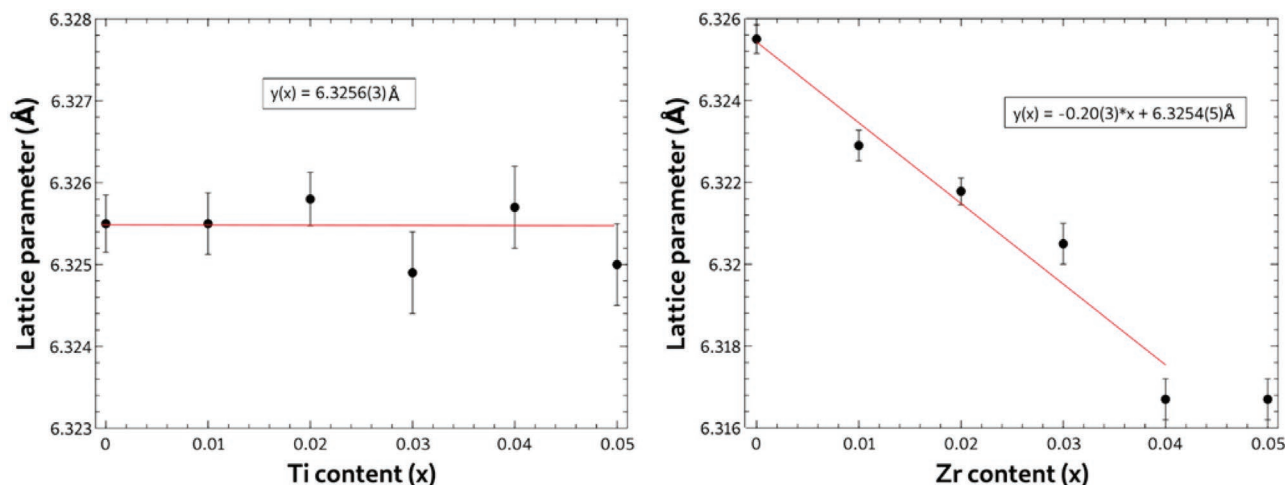


Figure 3. Evolution of the Le Bail refined lattice parameters for Sn_{1-x}Ti_xTe (left) and Sn_{1-x}Zr_xTe (right) series ($0 \leq x \leq 0.05$).

till 600 K for these optimized Ti ($x = 0.03$) and Zr-doped ($x = 0.02$) compositions. The thermal conductivities of Ti and Zr-doped SnTe compounds are presented in Figures 5d and 6d. Substitution of Ti or Zr for Sn in SnTe seems to suppress the thermal transport. The decreased thermal transport in both these Ti and Zr-doped systems stems from the suppression of both electronic (Figure S1, Supporting Information) and lattice contribution (Figures 5e and 6e) to the total thermal conductivity. The reduction in the electronic contribution to thermal conductivity with Ti/Zr addition is not surprising, given their tread with electrical conductivity. However, the suppression of lattice contribution to the thermal conductivity is quite striking, with κ_{latt} reaching as low as $\approx 1 \text{ W m}^{-1} \text{ K}^{-1}$ for both cases. Like

changes in electrical transport, the reduction in κ with varying dopant content is more prominent in Zr-series than Ti-series. For instance, at 323 K, κ decreases (reduction by about 47%) from $\approx 75 \text{ W m}^{-1} \text{ K}^{-1}$ for pristine SnTe to $\approx 4 \text{ W m}^{-1} \text{ K}^{-1}$ for the optimized Zr-doped (Sn_{0.98}Zr_{0.02}Te) composition. It is important to note that, not only those optimized compositions of Sn_{0.97}Ti_{0.03}Te and Sn_{0.98}Zr_{0.02}Te exhibit superior PF, but they also manifest the least κ (Figures 5d and 6d) in their respective series. Therefore, amongst the Sn_{1-x}Ti_xTe and Sn_{1-x}Zr_xTe series, the best trade-off-between σ , S and κ are obtained when $x = 0.03$ in the case of Ti-doping and when $x = 0.02$ in the case of Zr doping. Detailed explanations and reasons pertaining to the favorable changes in electrical and thermal transport with

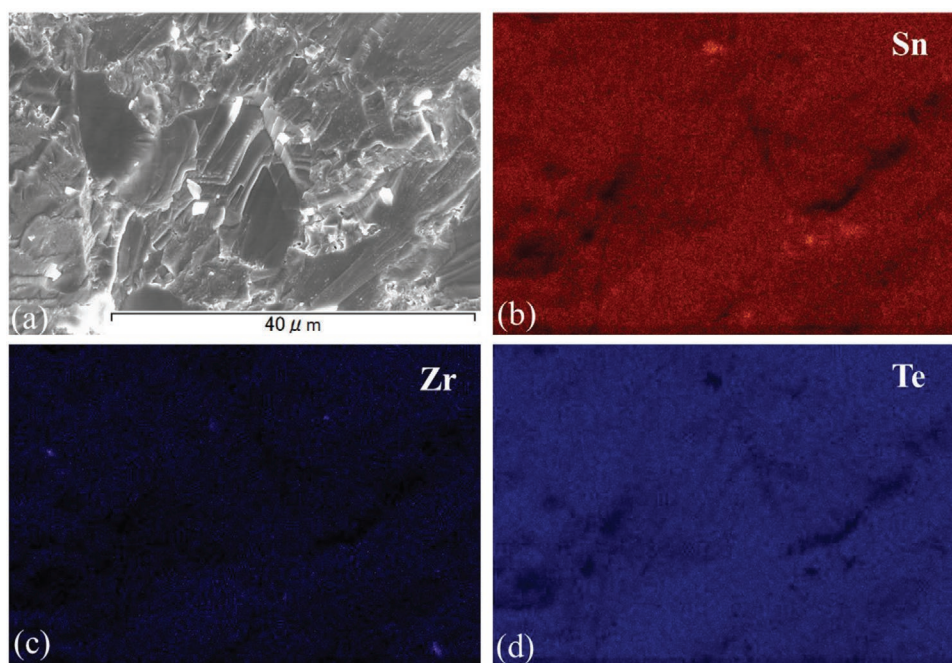


Figure 4. SEM image of a Sn_{0.98}Zr_{0.02}Te sample and b–d) its EDX chemical mapping of constituent elements—Sn, Zr, and Te.

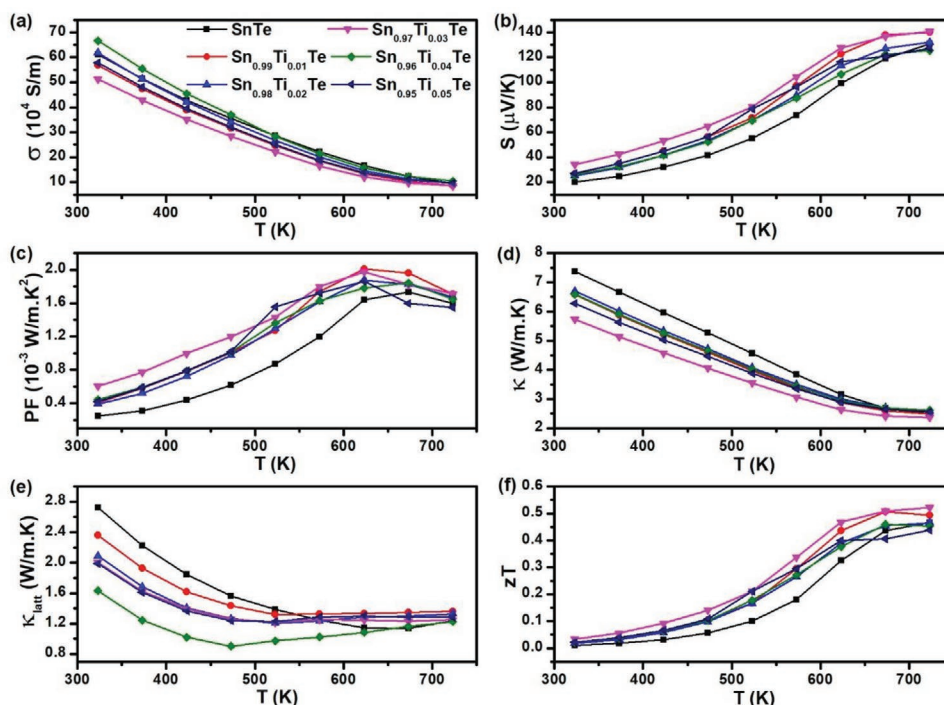


Figure 5. Temperature-dependent a) electrical conductivity (σ), b) Seebeck coefficient (S), c) power factor ($\text{PF} = S^2\sigma$), d) total thermal conductivity (κ), e) lattice thermal conductivity (κ_{latt}), f) figure of merit (zT) for $\text{Sn}_{1-x}\text{Ti}_x\text{Te}$ ($0 \leq x \leq 0.05$) series.

Ti or Zr's doping to SnTe are elaborated in the forthcoming sections (Sections 2.4 and 2.5) in the paper. The short inference from this section is that the cumulative effects of suppressed

thermal transport and enhanced power factor exhibited by these optimized compositions enabled them to possess substantially decent peak/maximum figure of merits, that is,

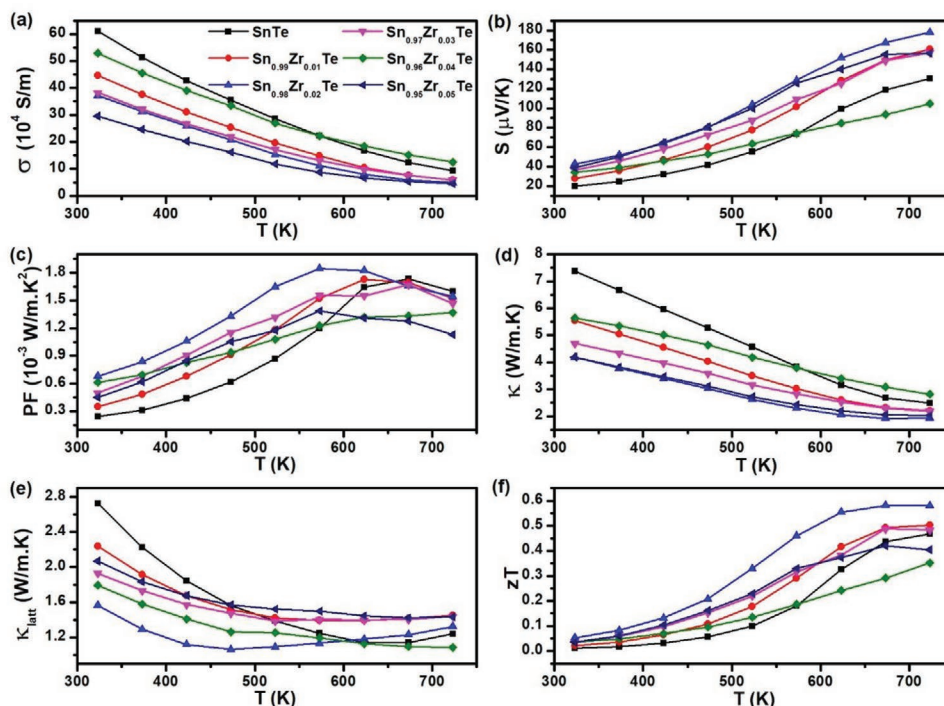


Figure 6. Temperature-dependent a) electrical conductivity (σ), b) Seebeck coefficient (S), c) power factor ($\text{PF} = S^2\sigma$), d) total thermal conductivity (κ), e) lattice thermal conductivity (κ_{latt}), f) figure of merit (zT) for $\text{Sn}_{1-x}\text{Zr}_x\text{Te}$ ($0 \leq x \leq 0.05$) series.

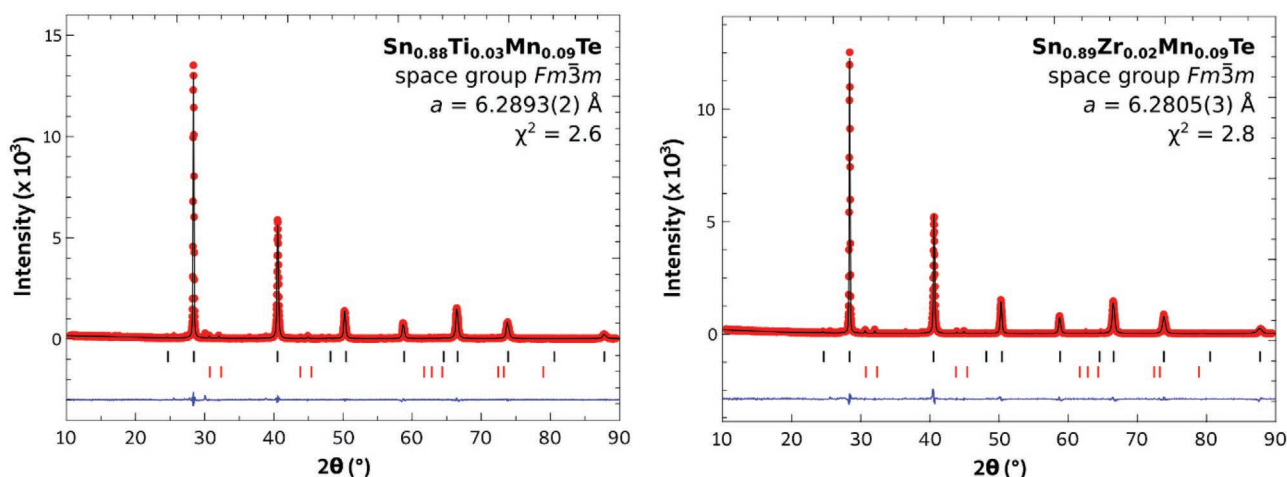


Figure 7. Le Bail refined room temperature XRD patterns of $\text{Sn}_{0.88}\text{Ti}_{0.03}\text{Mn}_{0.09}\text{Te}$ (left) and $\text{Sn}_{0.89}\text{Zr}_{0.02}\text{Mn}_{0.09}\text{Te}$ (right). The experimental pattern is plotted with red symbols, the calculated pattern with black lines, and the difference with blue lines. The vertical ticks indicate the Bragg positions of the SnTe phase (black) and secondary Sn phase (red).

$zT_{\text{max}} \approx 0.52$ at 700 K for $\text{Sn}_{0.97}\text{Ti}_{0.03}\text{Te}$, and $zT_{\text{max}} \approx 0.6$ at 700 K for $\text{Sn}_{0.98}\text{Zr}_{0.02}\text{Te}$, as depicted in Figures 5f and 6f, respectively, and an overall improvement in zT throughout the entire spectrum of temperature (323–723 K).

2.3. Structure and Transport Properties of Ti-Mn and Zr-Mn Codoped SnTe Compounds

To the optimized Ti and Zr-doped compositions, Mn was codoped to form the Ti-Mn and Zr-Mn codoped series, that is, $\text{Sn}_{1-x-y}\text{Ti}_x\text{Mn}_y\text{Te}$ ($x = 0.03$, $y = 0.09$) and $\text{Sn}_{1-x-y}\text{Zr}_x\text{Mn}_y\text{Te}$ ($x = 0.02$, $y = 0.09$). Specifically, the value of y is fixed as 0.09, as it was found to be the best-optimized composition in the Mn-doped SnTe system.^[53] The Le Bail refined XRD patterns for $\text{Sn}_{0.88}\text{Ti}_{0.03}\text{Mn}_{0.09}\text{Te}$ and $\text{Sn}_{0.89}\text{Zr}_{0.02}\text{Mn}_{0.09}\text{Te}$ are shown in Figure 7. In both the codoped systems (Ti-Mn and Zr-Mn), all the major reflections can be indexed to the SnTe phase, and like their single doped counterparts, some minor reflections corresponding to metallic Sn is also present. Upon doping with 9% Mn, the lattice parameters of $\text{Sn}_{0.97}\text{Ti}_{0.03}\text{Te}$ and $\text{Sn}_{0.98}\text{Zr}_{0.02}\text{Te}$ decrease significantly from 6.3247(2) to 6.2893(2) Å and from 6.3216(1) to 6.2805(3) Å, respectively, confirming the high solubility of Mn in $\text{Sn}_{1-x}\text{M}_x\text{Te}$ ($M = \text{Ti}$ or Zr) system. Such a decrease of the lattice parameter is consistent with the smaller ionic radius of Mn^{2+} (80 pm) substituting for Sn^{2+} (93 pm). The thermoelectric transport properties of these codoped compounds are compared with their optimized single doped and pristine SnTe, as shown in Figure 8. Codoping of Mn to $\text{Sn}_{1-x}\text{M}_x\text{Te}$ ($M = \text{Ti}$ or Zr) systems drastically changed their electrical and thermal transport properties. Though the electrical conductivity (Figure 8a) was decreased with Mn codoping, it was well compensated by the striking increase in Seebeck coefficient (Figure 8b). The sharp rise in S -values with Mn codoping is evident even at room temperature. For instance, at 323 K, the thermopower for pristine and single doped (Ti/Zr) compounds are less than $40 \mu\text{V K}^{-1}$, while it reached

$\approx 100 \mu\text{V K}^{-1}$ when Mn was codoped to those optimized compositions. This has led to a higher power factor for these Ti-Mn and Zr-Mn codoped SnTe compounds, albeit only at lower temperature region ($T < 500$ K), as depicted in Figure 8c. After 500 K, these PF values for these codoped compounds are stabilized, but lower than the PF values of single doped (Ti/Zr) optimized composition. Mn codoping has tremendously helped in suppressing the thermal transport, as can be seen from the total thermal conductivity results presented in Figure 8d. κ for $\text{Sn}_{0.88}\text{Ti}_{0.03}\text{Mn}_{0.09}\text{Te}$ and $\text{Sn}_{0.89}\text{Zr}_{0.02}\text{Mn}_{0.09}\text{Te}$ reaches as low as values below $1.5 \text{ W m}^{-1} \text{ K}^{-1}$ at $T > 600$ K. Not only at elevated temperature, but even at 323 K, these Mn codoped compounds exhibit low $\kappa \approx 2 \text{ W m}^{-1} \text{ K}^{-1}$, which is a reduction by 275% when compared with pristine SnTe. In particular, there has been a sharp decline in the lattice contribution to the thermal conductivity when Ti-Mn and Zr-Mn are codoped to the SnTe (Figure 8e). The resulting effect of this huge decrease in κ (throughout the whole temperature range) and gain in PF (at lower temperature regions) is that the figure of merit for these Ti-Mn and Zr-Mn codoped SnTe materials are further enhanced throughout the entire temperature range (Figure 8f). $zT_{\text{max}} \approx 0.7$ at 723 K is attained for both $\text{Sn}_{0.88}\text{Ti}_{0.03}\text{Mn}_{0.09}\text{Te}$ and $\text{Sn}_{0.89}\text{Zr}_{0.02}\text{Mn}_{0.09}\text{Te}$ compounds. From these results, it can be inferred that the PF increment in the lower temperature region plays a notable role, but the major factor assisting in boosting the TE performance in Mn-codoped systems comes from the suppressed κ . Factors contributing to these favorable changes in transport properties are elucidated in the upcoming sections. It must also be brought to the attention that the minor proportion of elemental Sn phase in SnTe did not affect much their transport properties. The results were fairly consistent during the heating and cooling cycles and reproducible (Figure S2, Supporting Information). To further support this fact, when the TE properties of pristine SnTe from this work (which contains Sn impurity phase) is compared with some literature reports where they do not detect any Sn secondary phase, their transport properties are quite comparable.^[48,64,65]

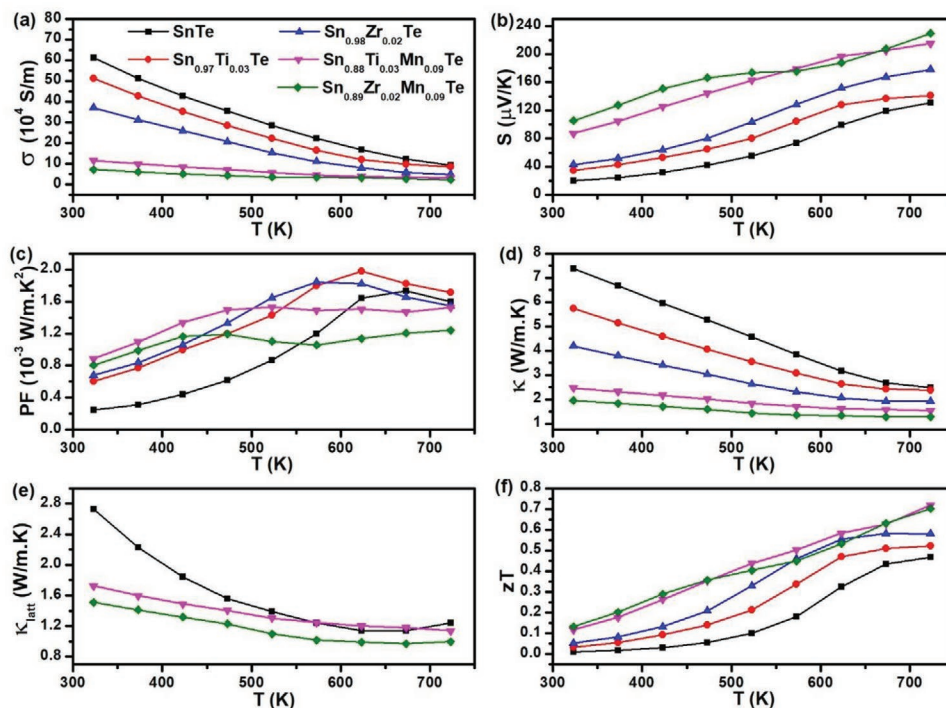


Figure 8. Temperature-dependent a) electrical conductivity (σ), b) Seebeck coefficient (S), c) power factor ($PF = S^2\sigma$), d) total thermal conductivity (κ), e) lattice thermal conductivity (κ_{latt}), f) figure of merit (zT) for Ti-Mn and Zr-Mn codoped SnTe compounds in comparison with the optimized Ti/Zr single doped and pristine SnTe. To avoid the overlap and to improve the readability, κ_{latt} of optimized single doped (Ti/Zr) SnTe is not given here in (e) (refer Figures 6e and 7e for the κ_{latt} of Ti/Zr doped SnTe).

2.4. Understanding the Reasons for Enhanced Electrical Transport in Ti/Zr Doped and Ti-Mn/Zr-Mn Codoped SnTe Systems

2.4.1. Discussion on Carrier Concentration, Mobility, Effective Mass, and Weighted Mobility—Validating Heikes's Equation as an Acceptable Method for Estimating Carrier Concentration and the Importance of Weighted Mobility as a Prime Thermoelectric Descriptor

To understand the variations in electrical transport with Ti/Zr doping to SnTe, their charge carrier concentrations (n) are estimated based on the modified Heikes' equation proposed by Taguchi et al. (in 1998),^[58]

$$n = \left[\frac{A_s}{V} \right] \left[\frac{1}{e^{(S \times e / (k_B))} + 1} \right] \quad (1)$$

where A_s/V is the number of available sites per unit volume of the unit cell (in this case, $A_s = 1$ for cubic SnTe system), and k_B , e , and S are the Boltzmann constant, electronic charge, and Seebeck coefficient, respectively. Using the standard electrical conductivity relationship (Equation (2)), the charge carrier mobility (μ) is calculated.

$$\sigma = ne\mu \quad (2)$$

From the values of S and n , the effective mass (m^*) is calculated based on the following relation,^[66]

$$S = \frac{8\pi^2 k_B^2}{3eh^2} (Tm^*) \left(\frac{\pi}{3n} \right)^{2/3} (1+r) \quad (3)$$

where h is the Planck constant, r is the scattering parameter. Generally, $r = 1/2$ for ionic solids.^[67] The calculated values for carrier density, mobility, and effective mass are presented in **Table 1**. It must be noted that the carrier concentration obtained from such an equation is much higher than what we usually get from Hall measurements, because the spin-orbit coupling and configurational entropy contributions are assumed to be negligible in Heikes' formula.^[58,68] Therefore, only the trend/tendency of these values given in **Table 1** must be considered and not their absolute values.

Aliovalent substitution of Ti^{4+} or Zr^{4+} to Sn^{2+} in SnTe decreased the charge carrier concentration (**Table 1**), and this explains the reason for these optimized $\text{Sn}_{0.97}\text{Ti}_{0.03}\text{Te}$ and $\text{Sn}_{0.98}\text{Zr}_{0.02}\text{Te}$ compounds to exhibit lower σ when compared to pristine SnTe (**Figure 8a**). The carrier concentration and mobility are relatively lower for the optimized Zr-doped compound when compared to the optimized Ti-doped compounds, which enlightens the relatively higher σ in $\text{Sn}_{0.97}\text{Ti}_{0.03}\text{Te}$ than $\text{Sn}_{0.98}\text{Zr}_{0.02}\text{Te}$. In the case of single doped systems, the major contribution to the enhancement in zT comes from their overall improvement in their PF. To understand the reason behind this, their trend on mobility (μ) and effective mass (m^*) must be carefully looked at, because once the carrier concentration is optimized, it is the weighted mobility (charge carrier mobility weighted by the density of electronic states) that governs the

Table 1. Modified Heikes' equation^[58] derived carrier concentration (n), carrier mobility (μ), effective mass (m^*) and weighted mobility (μ_w) for the SnTe-based compounds.

Composition	n [cm^{-3}]	μ [$\text{cm}^2 \text{V}^{-1} \text{s}^{-1}$]	m^*/m_e	μ_w [$\text{cm}^2 \text{V}^{-1} \text{s}^{-1}$]
SnTe	1.75×10^{21}	21.82	0.89	18.41
$\text{Sn}_{0.97}\text{Ti}_{0.03}\text{Te}$	1.59×10^{21}	20.17	1.44	34.82
$\text{Sn}_{0.98}\text{Zr}_{0.02}\text{Te}$	1.53×10^{21}	12.66	1.63	26.27
$\text{Sn}_{0.88}\text{Ti}_{0.03}\text{Mn}_{0.09}\text{Te}$	1.07×10^{21}	6.75	2.82	31.88
$\text{Sn}_{0.89}\text{Zr}_{0.02}\text{Mn}_{0.09}\text{Te}$	9.19×10^{20}	4.92	3.06	26.38

The effective mass (m^*) is given in m_e (m_e is the free electron mass). Considering the assumptions used in the modified Heikes' equation, only the tendency/trend must be analyzed and not the absolute values given in this table.

PF_{max} in a given material. The weighted mobility, μ_w is given by Equation (4),^[55]

$$\mu_w \approx \mu (m^*/m_e)^{3/2} \quad (4)$$

From Table 1 it can be seen that the weighted mobility (μ_w) substantially increased with the addition of optimum content of Ti/Zr to SnTe in the single doped systems. The favorable raise in PF for the single doped $\text{Sn}_{0.97}\text{Ti}_{0.03}\text{Te}$ and $\text{Sn}_{0.98}\text{Zr}_{0.02}\text{Te}$ compounds (Figure 8c) can thus be attributed to the right balance between the improved m^* and reduced μ when compared to pristine SnTe. Considering the assumptions used in the modified Heikes' equation to derive n (and hence μ_w), only the trend was looked at. Moreover, μ_w calculated using Equation (4) relies on the parabolic band and scattering assumptions.^[55]

To reconfirm the above stated factors as the reason behind the improved PF with Ti/Zr doping to SnTe, a more robust estimation of the temperature-dependent weighted mobility, μ_w is calculated based on the recently proposed (in 2020) formulae by Snyder et al.,^[55] that approximates the exact Drude–Sommerfeld free electron model,

$$\mu_w = \frac{3h^3\sigma}{8\pi e(2m_e k_B T)^{3/2}} \left[\frac{\exp\left[\frac{|S|}{k_B/e} - 2\right]}{1 + \exp\left[-5\left(\frac{|S|}{k_B/e} - 1\right)\right]} + \frac{3}{\pi^2} \frac{|S|}{k_B/e}}{1 + \exp\left[5\left(\frac{|S|}{k_B/e} - 1\right)\right]} \right] \quad (5)$$

where h , k_B , e and other notations were already defined in the previous equations.

In Equation (5), non-parabolic, multi-band, and other scattering effects are not neglected, and μ_w acts as a parameter that directly represents the electronic qualities in a given material. The temperature-dependent weighted mobility obtained based on the above equation for the optimized Ti/Zr-doped SnTe is presented in Figure 9. μ_w decreases with temperature, suggesting that the charge carriers are scattered by phonons, as like in any ideal thermoelectric material. The increase/decrease of μ_w at different/specific temperature regimes depends on a lot of factors such as disorder, micro-structure (grain boundary), ionized impurity scattering, and acoustic or deformation potential phonon scattering.^[69–71] Clearly, for most of the low to the mid-temperature regime, μ_w for the $\text{Sn}_{0.97}\text{Ti}_{0.03}\text{Te}$ and $\text{Sn}_{0.98}\text{Zr}_{0.02}\text{Te}$ compounds are higher than the

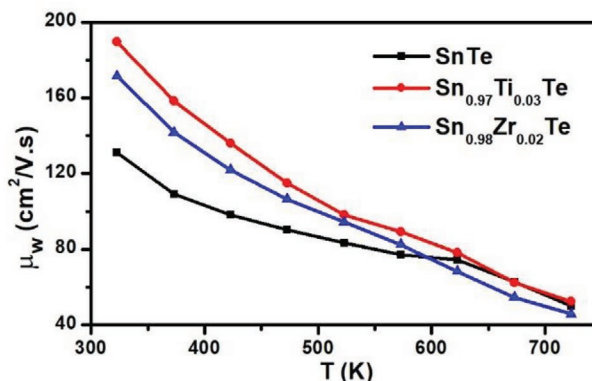


Figure 9. Temperature-dependent experimental weighted mobility (μ_w) for $\text{Sn}_{0.97}\text{Ti}_{0.03}\text{Te}$ and $\text{Sn}_{0.98}\text{Zr}_{0.02}\text{Te}$ compounds in comparison with pristine SnTe. The trend of experimental μ_w in this figure (μ_w calculated from experimental S , σ , as proposed by Snyder et al.^[55]) is consistent with the trend of μ_w given in Table 1 (μ_w calculated based on n , μ derived from modified Heikes' relation^[58]).

pristine SnTe. Significantly, the trend that is obtained here, that is, μ_w of $\text{Sn}_{0.97}\text{Ti}_{0.03}\text{Te} > \text{Sn}_{0.98}\text{Zr}_{0.02}\text{Te} > \text{SnTe}$, that is based on Equation (5) is consistent with the μ_w trend obtained based on Heikes' equation (Table 1). Therefore it can be safely concluded that the reasons that are proposed in the earlier paragraph for the enhanced thermoelectric power factor with the addition of optimum content of Ti/Zr to SnTe (right balance between the improved m^* and optimized n , μ) seem valid/hold good.

From a broader perspective, the results and discussion presented in this particular sub-section opens the argument on two general fronts for the thermoelectric (TE) scientific community: i) Modified Heikes' equation proposed by Taguchi et al.,^[58] which is hardly applied within the TE research, as a reliable method to estimate or at least to compare the trend of charge carrier concentration of TE materials. Typically, a TE material's carrier concentration and mobility are measured using the Hall effect (in a magnetic field) and electrical resistivity. When one looks at the Starry-Data2, an extensive database developed by Y. Katsura et al.,^[72] abundant information is available on the transport properties of TE materials, but only a few of them have reported the Hall effect data. Moving forward, considering the limitations with Hall measurements (access to facilities, contact issues with the van der Pauw method, sample geometry constraints, etc.), modified Heikes' equation could be a vital alternative option that the TE community can seriously consider and discuss, at least for materials with simple crystal structures. ii) Temperature-dependent weighted mobility (Equation (5)) calculated directly from the experimental values of S and σ ,^[55] as a more reliable descriptor of the electrical transport properties (power factor) of a given material, as it is more independent of Hall mobility/carrier concentration and magnetic impurities, as proposed very recently by Snyder et al.^[55]

2.4.2. Carrier Scattering Effects

An ideal compound that perfectly follows the Drude–Sommerfeld model with a parabolic band should not have

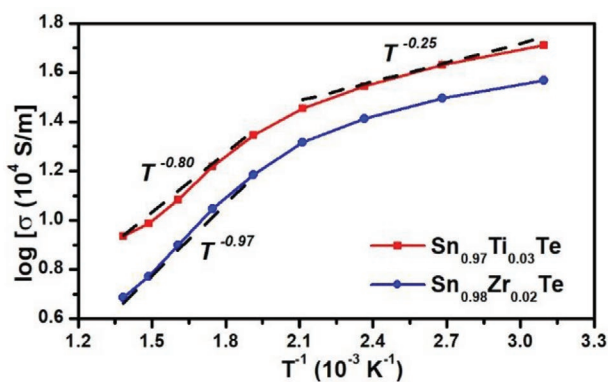


Figure 10. Temperature-dependent carrier scattering exponential ($\log[\sigma]$ vs $1/T$) for optimized Ti/Zr-doped SnTe compounds.

any variations in weighted mobility, μ_w upon doping.^[55] However, in this case, with the doping of Ti/Zr, μ_w of SnTe has favorably increased (Figure 9 and Table 1), and this could be due to some intricacies in the electronic band structure or scattering mechanisms. To have some insights on the carrier scattering mechanisms, the power-law plot of electrical conductivity, that is, $\log[\sigma]$ versus $1/T$ for the optimized $\text{Sn}_{0.97}\text{Ti}_{0.03}\text{Te}$ and $\text{Sn}_{0.98}\text{Zr}_{0.02}\text{Te}$ compounds is presented in **Figure 10**. At the mid-low temperature regime, the $\log[\sigma]$ for the optimized Ti/Zr doped compositions display $T^{-0.25}$ dependence, suggesting the possibilities for “mixed scattering mechanisms” in this low-temperature domain, which is known to dominate when the temperature exponent reaches close to 0.^[73–75] At a higher temperature regime, a steep reduction of $\log[\sigma]$ is observed with a larger slope ($\approx T^{-0.8} - T^{-0.97}$), which can be attributed to the additional acoustic phonon scattering, as the phonon concentration (n_{ph}) generally increases with T .^[75,76] Thus, the mixed scattering mechanisms can explain the rationale behind increased μ_w (Figure 9) especially at the mid-low temperature ranges). In the past, such strategical tuning of carrier scattering mechanisms has been reported to improve the PF for n -type Mg_3Sb_2 -based materials, where the mobility was enhanced by converting the ionized scattering into mixed scattering between

ionization ($\sigma \propto T^{1.5}$) and acoustic phonon scattering ($\sigma \propto T^{-1.5}$), which less effectively scatters the carriers.^[75]

2.4.3. Electronic Band Structural Effects

To explore the effects of dopant substitution (Ti/Zr/Mn) on the electronic density of state and/or band structure of SnTe, DFT calculations were performed on the cubic models of $\text{Sn}_{32}\text{Te}_{32}$ (SnTe), $\text{Sn}_{31}\text{TiTe}_{32}$ ($\text{Sn}_{0.97}\text{Ti}_{0.03}\text{Te}$), $\text{Sn}_{63}\text{ZrTe}_{64}$ ($\text{Sn}_{0.98}\text{Zr}_{0.02}\text{Te}$), $\text{Sn}_{28}\text{TiMn}_3\text{Te}_{32}$ ($\text{Sn}_{0.88}\text{Ti}_{0.03}\text{Mn}_{0.09}\text{Te}$) and $\text{Sn}_{57}\text{Zr}_1\text{Mn}_6\text{Te}_{64}$ ($\text{Sn}_{0.89}\text{Zr}_{0.02}\text{Mn}_{0.09}\text{Te}$) that closely represent the optimized experimental compositions, and their results are presented in **Figures 11–14**. The pristine SnTe (Figure 11a,b) has a narrow direct band gap (E_g), which is conducive for the transport of charge carriers from the highest occupied valence band (VB) to the lowest unoccupied conduction band (CB), and as the energy $k_B T \approx 0.026$ eV, the fraction of the thermally excited electrons is abundant enough to provide a high electrical conductivity (Figure 8a). The GGA computational approach is known to underestimate the values of the bandgap. In any case, the shape and trend of the bands computed from the GGA calculations are considered to be reliable. In this paper, only the DFT results based on GGA are presented and compared. However, to verify the reliability of the results, few calculations were also performed using the modified Becke and Johnson (mBJ) method,^[77] which are shown in Figures S3–S5, Supporting Information, and both those results (GGA and mBJ) were found to be quite consistent. Bandgaps calculated from the experimental Seebeck coefficient based on the Goldsmid–Sharp’s relation^[78] (Equation (6)) is given in **Table 2**

$$E_g \approx 2e|S_{\text{max}}|T_{\text{max}} \quad (6)$$

where T_{max} is the temperature at which the maximum thermopower, $|S_{\text{max}}|$ occurs, while e is the charge of the electron. The value computed on the primitive cell of SnTe is given in SI (Figures S4 and S5, Supporting Information). VB and CB edges possess almost the same magnitude of the density of states (Figure S4, Supporting Information), confirming the simple

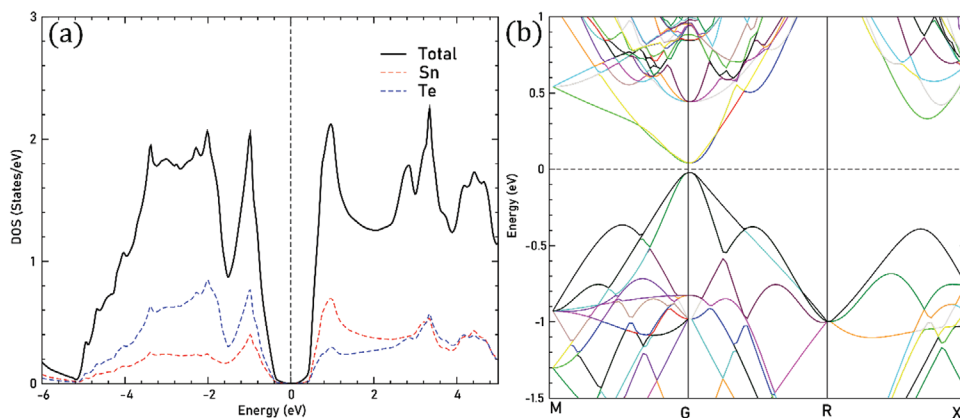


Figure 11. First-principles computed a) DOS, and b) band structure for pristine $\text{Sn}_{32}\text{Te}_{32}$ model (cubic). The Fermi level, E_F (shown in dashed lines) is set arbitrarily at 0 eV.

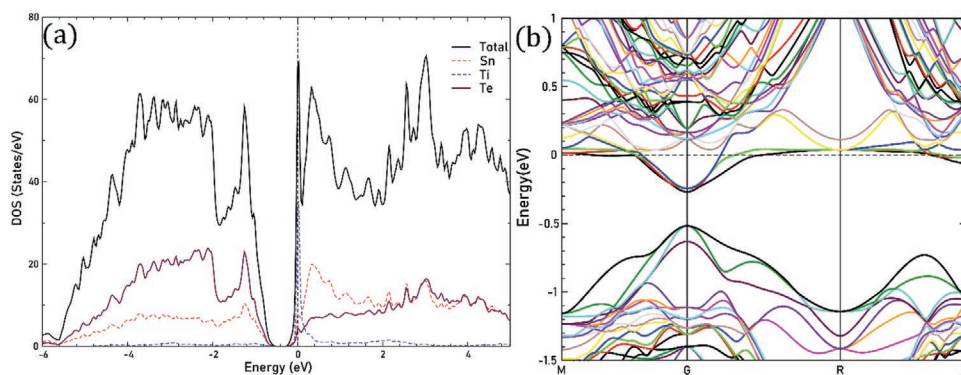


Figure 12. First-principles computed a) DOS, and b) band structure for $\text{Sn}_{31}\text{TiTe}_{32}$. The dashed lines at 0 eV represents the shifted Fermi level, E_F .

nature of the electronic structure of pristine SnTe, thus it is no wonder why they exhibit such a low thermopower (Figure 8b). The top of VB and bottom of CB (Figure S5, Supporting Information) have a non-degenerate single band (with narrow-band curvature), which can justify the low effective mass of pristine SnTe (Table 1). Though several bands may contribute to the transport properties, the key information lies at the valence band maximum located at Γ (corresponding to the light hole band) and the one located along with $R \rightarrow X$ direction (Σ) in the Brillouin zone (corresponding to the heavy hole band). The energy separation between these light and heavy hole valence bands ($\Delta E_{L\Sigma}$) for pristine SnTe was found to be quite large (≈ 0.4 eV), in agreement with the literature reports.^[37,79] When Ti substitutes for Sn, a pseudo-bandgap feature with a finitely large density of state (sharp peak from Ti-contribution) near the vicinity of the band edge is observed (Figure 12a). According to Mott's relationship, the increase of the density of states, especially near the Fermi-level (E_F), can contribute to an improvement in the Seebeck coefficient.^[80] More importantly, doping Ti to SnTe, simultaneously opens up the band gap at Γ point and promotes band convergence by decreasing the energy separation ($\Delta E_{L\Sigma}$) between the light hole and heavy hole valence bands (Figure 12b). The Zr-contribution to the DOS

(Figure 13a) of SnTe may not be as prominent as Ti, but it has certainly modified the band structure by activating many electronic pockets at several high symmetry points in the Brillouin zone (M, Γ, Z, X). This explains the increased effective mass, m^* , associated with these electronic pockets (Table 1), and thus the enhanced Seebeck coefficient with Zr-doping to SnTe (Figure 8b), as these electron/hole pockets located at the degenerated directions of the Fermi surface dictate the electrical transport in a given material.^[81] It can thus be stated that, with Zr-doping to SnTe, carrier-pockets have been optimized to enhance the power factor (Figure 8c). Indeed, carrier-pocket engineering is an effective strategy to simultaneously enhance both S and σ , especially employed on materials such as Half-Heusler (HH) compounds.^[82] Both Ti^{4+} and Zr^{4+} , when substitutes for Sn^{2+} in SnTe, shift E_F upward or into the conduction band. Previous DFT calculations have clearly demonstrated the role of Mn doping in SnTe, *i.e.*, it opens up E_g and decreases $\Delta E_{L\Sigma}$.^[53,83] When Ti/Zr is codoped to Mn, co-adjutant or synergistic band effects are brought into play due to the significant interaction between the substituted transition (Ti/Zr and Mn) atoms (Figure 14). For Zr-Mn codoped SnTe, the bandgap is reduced and the DOS is non-zero within the bandgap. The formation or appearance of the DOS near the vicinity of the

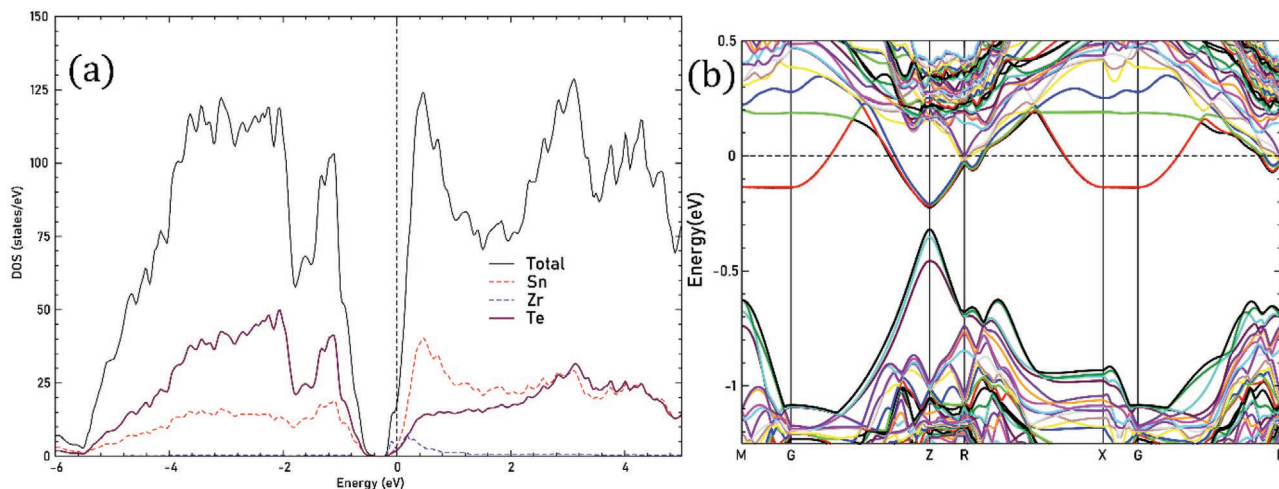


Figure 13. First-principles computed a) DOS, and b) band structure for $\text{Sn}_{63}\text{ZrTe}_{64}$.

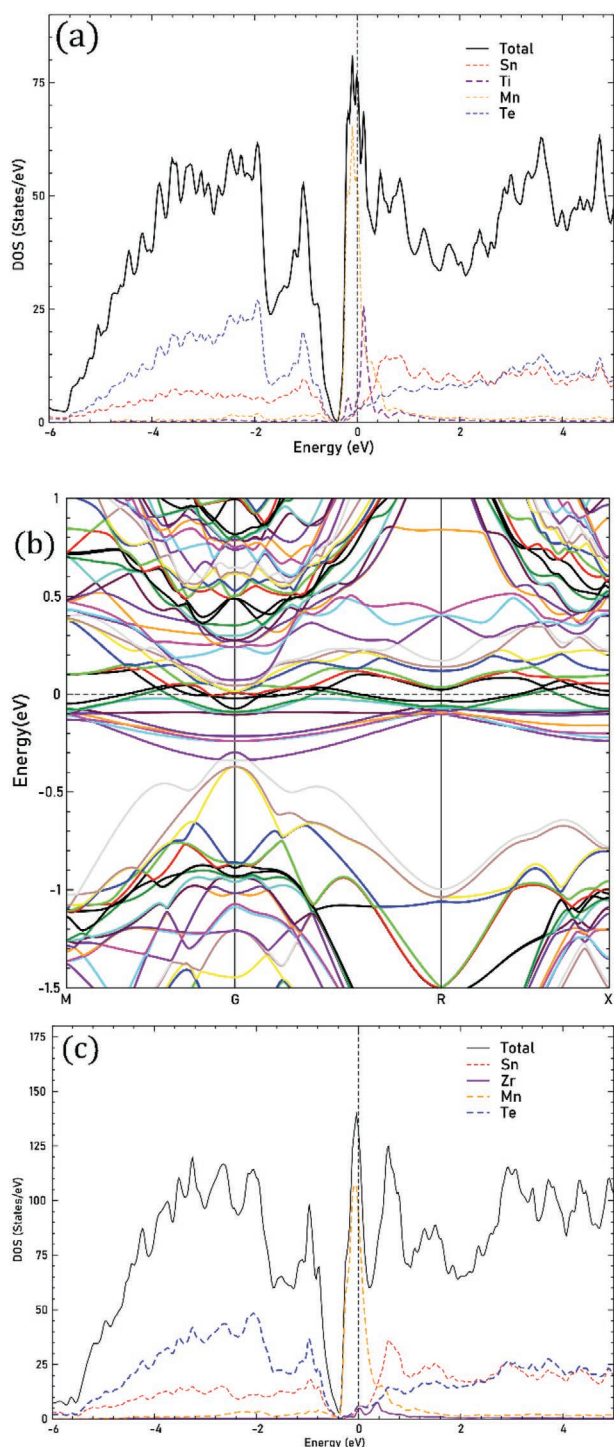


Figure 14. First-principles computed a) DOS, b) band structure for $\text{Sn}_{28}\text{TiMn}_3\text{Te}_{32}$, and c) DOS for $\text{Sn}_{57}\text{ZrMn}_6\text{Te}_{64}$.

chemical potential with Zr-Mn addition to SnTe suggests a semi-metallic band structure character (Figure 14c). Ti/Zr-Mn codoping to SnTe has resulted in adding donor states in the vicinity of E_F just below the conduction band edge. The band structure for codoped SnTe (Figure 14b) shows a combination of highly dispersive (valence and conduction bands) and

Table 2. Bandgaps (E_g) calculated from the maximum (experimental) thermopower based on the Goldsmid–Sharp’s relation.^[78]

Composition	E_g [eV]
SnTe	0.19
$\text{Sn}_{0.97}\text{Ti}_{0.03}\text{Te}$	0.20
$\text{Sn}_{0.98}\text{Zr}_{0.02}\text{Te}$	0.26
$\text{Sn}_{0.88}\text{Ti}_{0.03}\text{Mn}_{0.09}\text{Te}$	0.31
$\text{Sn}_{0.89}\text{Zr}_{0.02}\text{Mn}_{0.09}\text{Te}$	0.33

flat bands (dopant induced bands in the gap). Such a mixture of the overall flatness and the corrugation of the electronic bands (which can be together referred to as “corrugated flat bands”) should yield multiple Fermi surfaces (which are scattered across the entire Brillouin zone),^[84] and can potentially boost the thermopower, as observed experimentally for Ti-Mn and Zr-Mn codoped SnTe samples (Figure 8b). The phenomenon of coexistence of such flat and corrugated bands near E_F contributing to the enhanced thermoelectric performance has not been reported so far for any of the SnTe-based materials, thus providing an exciting prospect for future exploration in this direction (for SnTe thermoelectrics). In the past, the corrugated flat-band driven improved power factor has, however, been reported for materials such as RFeO_3 (wide bandgap), where $R = \text{Pr, Nd, Sm, and Gd}$,^[85] and PtSb_2 .^[84]

2.4.4. Magnetic Coupling

Besides the band convergence effect, Mn-doping to SnTe reported by Acharya et al.^[86] has been shown to induce weak ferromagnetism at low temperatures in an otherwise diamagnetic SnTe, which can give magnetic entropy and structural disorder leading to the modifications in transport properties. Such increase in magnetic moments (leading to the coupling of charge carriers) has resulted in the raise in the effective thermal mass of charge carriers in $\text{Sn}_{1-x}\text{Mn}_x\text{Te}$ systems.^[86] Therefore, the possible reasons of the increased magnetic moment, high effective thermal mass, the coupling of charge carriers with magnetic entropy cannot be ruled out in these cases of Ti-Mn and Zr-Mn codoped SnTe, and it provides further justification for their improved thermopower and power factor values, especially at the lower temperature region (Figures 8b,c). Indeed, the concept of magnetic ion introduction to enhance the power factor by balancing between the rise in effective mass and suppression of carrier mobility has been well documented in materials such as $\text{Bi}_{2-x}\text{Cr}_x\text{Te}_3$ ^[87] and $\text{CuGa}_{1-x}\text{Mn}_x\text{Te}_2$.^[88,89] In the past, ferroelectric instability engineering has even yielded ultra-low κ in crystalline solids, particularly in the $\text{Sn}_{1-x}\text{Ge}_x\text{Te}$ system^[90] and in $\text{Sn}_{1-x}\text{Mn}_x\text{Te}$ system.^[91] Therefore, the anticipated increase in the SnTe system’s magnetic entropy with Mn codoping with Ti/Zr can influence the electrical transport and play a role in their thermal behavior. This angle could further be explored/validated with magnetic measurements and low-temperature specific heat experiments on Ti-Mn and Zr-Mn codoped SnTe samples, making it an exciting avenue for potential future work.

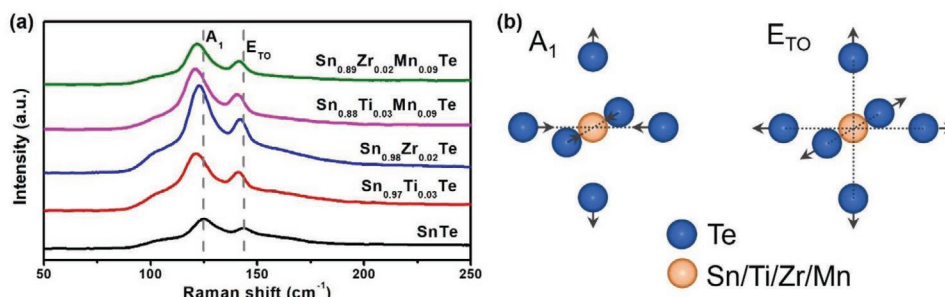


Figure 15. a) Raman spectra for Ti/Zr doped and Ti-Mn/Zr-Mn codoped compounds in comparison with pristine SnTe showing the shift of A_1 and E_{T0} vibrational modes to lower wavenumbers (Red shift), b) schematic representation of A_1 and E_{T0} vibrational modes for SnTe.

2.5. Understanding the Reasons for Suppressed Thermal Transport in Ti/Zr Doped and Ti-Mn/Zr-Mn Codoped SnTe Systems

2.5.1. Lattice Softening—Perspectives from Raman Analysis

To understand the origin of low thermal conductivity in the single doped (Ti/Zr) and codoped (Ti-Mn/Zr-Mn) SnTe systems, their phonon vibration properties were investigated using Raman spectroscopy. **Figure 15a** shows a typical Raman spectrum for pristine SnTe with two vibrational modes centered at ≈ 125 and ≈ 144 cm^{-1} , consistent with previous observations.^[92,93] The peak at 125 cm^{-1} corresponds to the optical phonon (A_1) mode, and the other at 144 cm^{-1} corresponds to the transverse optical phonon (E_{T0}) mode, and they represent the actual chemical bond environment around Te (Figure 15b). With the doping of Ti/Zr or codoping of Ti-Mn/Zr-Mn to SnTe, both A_1 and E_{T0} modes visibly shift toward the lower wavenumber/frequency, that is, to the lower energy region, generally termed as “red shift” effect, as the frequency of phonons interacting with the incident photon get decreased. In this context, the Raman shift indicates that the force constant of Te-Sn/M bonds (M = dopant—Ti/Zr/Mn) is altered. The vibrational model from classical physics relates the vibrational frequency of phonon (f) to the force constant of the chemical bond (K) using the relation, $f \approx (K/M)^{1/2}$, where M is the reduced mass of the material. M decreases when a light element (dopant) substitutes for a heavy element (host). Based on this relation, when Ti/Zr/Mn with lower mass than Sn substitutes in SnTe, one would expect the Raman peaks to shift toward higher frequency (“blue shift” effect), but what we observe (Figure 15a) is the opposite effect (red shift). Though not common, such a phenomenon has been reported in the past for SnTe-based materials.^[54,64,93] With the incorporation of Ti/Zr/Mn in SnTe, the red shift/low-frequency shift in the Raman spectra conveys that the force constant of the bonds around the Te site is reduced or the chemical bond is notably softened, as the bond stiffness is inversely proportional to bond length. This softening effect can well explain the reason for decreased lattice thermal conductivity when Ti/Zr or Ti-Mn/Zr-Mn are doped to SnTe.

The overall low frequency optical phonons resulting due to the weakening of the bonds (lattice softening) can also retard the frequency of acoustic phonons, and this conjoin effect between the acoustic and optical phonons can induce “rattling-like”

thermal damping,^[54] which in turn can affect the phonon group velocities and the overall lattice contribution to the thermal conductivity.

2.5.2. Lattice Softening Effect on the Phonon Group Velocity

To reconfirm these conclusions from Raman, the average phonon group velocities (v_g) have to be deduced from the phonon dispersion computations. However, the more convenient way is to measure the sound velocity (v_s) in the samples, as the average group velocity over the Brillouin zone, v_g is proportional to v_s . Refer to the materials and methods section for details regarding the measurements of the speed of sound in longitudinal (v_L) and transverse (v_T) directions in a material. The crystallographic average sound velocity (v_s) was then calculated using the following equation:^[24]

$$v_s = \left[\frac{1}{3} \left(\frac{1}{v_L^3} + \frac{2}{v_T^3} \right) \right]^{-1/3} \quad (7)$$

The measured v_s (using a pulse-echo technique) for the pristine and doped SnTe compounds are presented in **Table 3**. For undoped SnTe, $v_s \approx 2143$ m s^{-1} , consistent with the previous reports,^[94] and it ranges between 2041–2097 m s^{-1} for the optimized Ti/Zr-doped SnTe, and further down to 2004–1957 m s^{-1} for the Ti-Mn/Zr-Mn-codoped SnTe. The clear decline in the phonon group velocity (v_s used as an estimate of v_g) of SnTe with the incorporation of Ti/Zr and Ti-Mn/Zr-Mn substantiates the lattice softening effect, predicted previously from the Raman spectral analysis. This once again substantiates the

Table 3. Speed of sound measured using pulse-echo ultrasound technique for SnTe-based samples.

Composition	v_L [m s^{-1}]	v_T [m s^{-1}]	v_s [m s^{-1}]
SnTe	3451	1925	2143
$\text{Sn}_{0.97}\text{Ti}_{0.03}\text{Te}$	3419	1881	2097
$\text{Sn}_{0.98}\text{Zr}_{0.02}\text{Te}$	3402	1828	2041
$\text{Sn}_{0.88}\text{Ti}_{0.02}\text{Mn}_{0.09}\text{Te}$	3398	1792	2004
$\text{Sn}_{0.89}\text{Zr}_{0.02}\text{Mn}_{0.09}\text{Te}$	3352	1749	1957

reduction in lattice thermal conductivity, as v_g is directly related to κ_{latt} , which is primarily an integration of the spectral thermal conductivity over the entire frequency (ω) range, given by the Equation (8),^[95]

$$\kappa_{\text{latt}} = \frac{1}{3} \int_0^{\omega_{\text{max}}} C_s v_g^2 \tau d\omega \quad (8)$$

where C_s is the spectral heat capacity and τ is the phonon relaxation time.

It is essential to diagnose that even a tiny change in v_s (i.e., v_g) can induce a significant change in κ_{latt} . Such intense dependence of κ_{latt} on v_s were observed in the past for lattice softened PbTe.^[56]

2.5.3. Possible Phonon Scattering Effects

From the previous sections, it is can be stated with confidence that the lattice softening effect accounts for the majority reduction in thermal transport in these Ti/Zr and Ti-Mn and Zr-Mn doped SnTe materials. Though this lattice softening effect is the main player in the reduction of κ_{latt} in these doped SnTe compounds, the conventional phonon scattering contribution cannot be ignored entirely, especially at high-temperature ranges. To support this, a plethora of information is available in the literature (based on TEM analysis) to show that doping of elements (especially Mn) to SnTe can cause multi-scale hierarchical structural defects,^[28,29,41,53] including a high density of point-defects, planar stacking faults, atomic-scale interstitials, dislocations (ordered/disordered), strain clusters, phase boundary between different scales of precipitates, all of which can effectively scatter phonons of different wavelengths or mean free paths. Due to these past well-established (and incrementally reported) findings on the nanostructural aspects of the doped-SnTe system, TEM images are not presented in this work. However, the shreds of evidence of these defects in the studied Ti/Zr doped and Ti-Mn/Zr-Mn codoped SnTe samples are corroborated based on the X-ray diffraction data (internal strain analysis) in the later sub-section [sub-section 2.5.6. Besides TEM, several lattice thermal conductivity/phonon

transport models, such as the Debye-Callaway model and Klemm's models, where all the contributing factors are taken into account, that is, Umklapp process, point defect scattering, grain boundary scattering, dislocation core scattering, dislocation strain scattering, interstitial scattering, and so forth, carried out on SnTe-based compounds (especially on Mn-doped ones),^[24,41,53] clearly establishes the role of these multi-scale features in phonon scattering and in subsequent κ_{latt} reduction. Such high-quality SnTe compounds, if influenced partially or completely by the anharmonic phonon-phonon scattering (Umklapp process), are known to exhibit a linear dependence of κ_{latt} as a function of $1000/T$,^[93,96] which is exactly what we observe for the Ti-Mn and Zr-Mn codoped SnTe systems, as shown in **Figure 16**.

2.5.4. Lattice Softening versus Phonon Scattering on κ_{latt} Reduction in Ti/Zr/Mn-Doped SnTe—Qualitative Standpoint from a Physical Model

In this case, to qualitatively assess the contributions from lattice softening and phonon scattering on κ_{latt} reduction, a model based on the previous work on PbTe,^[56] has been used. The commonly used phonon-phonon expression for scattering (τ_{pp}) at high temperature is given in Equation (9),^[97]

$$\tau_{\text{pp}} = \left(\frac{6\pi^2}{V} \right)^{1/3} \frac{\overline{M} v_g v_p^2}{2k_B \gamma^2 \omega^2 T} \quad (9)$$

where phonon group velocity, $v_g = d\omega/dk$, and its phase velocity, $v_p = \omega/k$, and \overline{M} , V , γ are the average atomic mass and volume, and Grüneisen parameter, respectively. At high temperatures, when phonon-phonon scattering dominates, that is, $T >$ Debye temperature, θ_D , and $\tau = \tau_{\text{pp}}$, then the spectral heat capacity and the resulting lattice contribution to the thermal conductivity can be given by the Equations (10) and (11), respectively:^[97]

$$C_s(\omega) = \frac{3k_B \omega^2}{2\pi^2 v_g v_p^2} \quad (10)$$

$$\kappa_{\text{latt}} = \frac{(6\pi^2)^{2/3} \overline{M} \langle v_g^3 \rangle}{V^{2/3} 4\pi^2 \gamma^2 T} = A \frac{v_s^3}{T} \quad (11)$$

Equation (11), derived by Hanus et al.^[56] (demonstrated for PbTe), will more or less give the same result as the spectral Callaway model and the Born-von Karman approximation model that was used by Tan et al. for SnTe-AgSbTe₂ alloys.^[94] For a holistic description and validity of this model, kindly refer to the recent work by Hanus et al.^[56] In Equation (11), the average atomic mass \overline{M} , atomic volume V , and Grüneisen parameter γ ($\gamma \approx 2.1$ for SnTe^[41,53]), are consolidated into a pre-factor A , which is normalized to pristine SnTe and held constant for a given material system in order to enable v_s as the ultimate decisive parameter of this model. It must be noted that the utilization of v_s in this $\kappa_{\text{latt}} = A v_s^3 T^{-1}$ modeling relation is based on the presumption that the variation in a material's speed of sound will reflect the average variation in the group velocity through the Brillouin zone. The results of this modeling process, shown

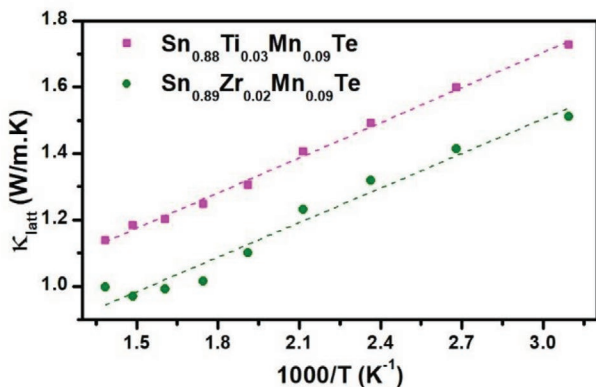


Figure 16. Lattice thermal conductivity as a function of $1000/T$ showing a linear dependence for $\text{Sn}_{0.88}\text{Ti}_{0.03}\text{Mn}_{0.09}\text{Te}$ and $\text{Sn}_{0.89}\text{Zr}_{0.02}\text{Mn}_{0.09}\text{Te}$ samples.

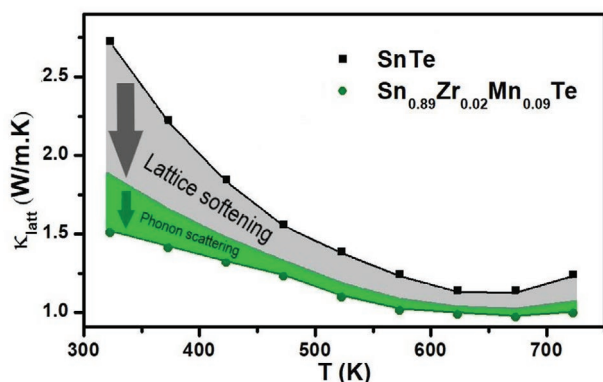


Figure 17. Estimation of the contributing factors affecting the lattice thermal conductivity based on the model,^[56] $\kappa_{\text{latt}} = Av_s T^{-1}$. A is normalized to pristine SnTe and fixed, and the only difference in the model between pristine SnTe and Zr-Mn codoped SnTe is the measured sound velocity, v_s . The grey region shows the reduction in κ_{latt} expected from lattice softening alone (without assuming any rise in phonon scattering centers) on addition of Zr-Mn to SnTe. The phonon scattering accounts for the remaining reduction in κ_{latt} for Zr-Mn codoped SnTe (shown as green region). The shaded regions (grey and green) are only a qualitative representation (based on the model approximation) to give an illustrative idea about the contributing factors.

in **Figure 17** approximately/qualitatively gives the effects of lattice softening and phonon scattering on the lattice thermal conductivity. It is indeed the lattice softening effect (shown in the “grey” shaded region in **Figure 17**) that primarily accounts for the reduction in κ_{latt} in Zr-Mn-codoped SnTe, as foreseen/consistent with the analysis of Raman and sound velocity measurements. The relatively less dominant phonon scattering (shown in the “green” shaded region in **Figure 17**) plays the second fiddle in further suppressing the lattice thermal conductivity in the Zr-Mn-codoped SnTe.

2.5.5. Analogies from Elastic Properties—Shear and Young’s Moduli versus Phonon Anharmonicity

Elastic properties of a material can present a window/insight into phonons’ behavior and give an estimate of their anharmonicity. Since SnTe-based materials are cubic and isotropic, their elastic constants are calculated based on Equations (12)–(14).^[98,99] The bulk modulus (B) is given by

$$B = \rho \left(v_L^2 - \frac{4}{3} v_T^2 \right) \quad (12)$$

The shear modulus, G is calculated as follows:

$$G = v_T^2 \rho \quad (13)$$

where v_L and v_T are the speed of sound in the longitudinal and transverse directions, respectively, and ρ is the density of the material. As the theoretical densities of the studied samples are close to the measured densities, any potential effects of density variations on the calculation of elastic constants can be excluded.

The Young’s modulus, Y is given by the following relation:

$$Y = \frac{9BG}{3B + G} \quad (14)$$

The elastic moduli G and Y for pristine, Ti/Zr single-doped, Ti-Mn, and Zr-Mn codoped SnTe samples are presented in **Table 4**. Note that the elastic properties (and sound velocities) calculated for these SnTe-based polycrystalline materials represent an average over all crystallographic directions. The obtained elastic moduli for pristine SnTe (presented in **Table 4**) is comparable with the shear and Young’s moduli calculated using the Hashin–Strikman (H–S) bounds method (without crystallographic textures).^[46] Generally, the elastic moduli of solids decrease when the unit cell volume increase.^[100] As the addition of Ti/Zr/Mn to the SnTe system decreases the unit cell volume (refer the XRD results in **Figures 3 and 7**), one would expect a raise in elastic moduli. However, it is the contrary here, where the elastic moduli (both shear and Young’s) show a decreasing trend with the addition of Ti/Zr/Mn to the SnTe system (**Table 4**). This contrary behavior (i.e., softening of elastic moduli) is consistent with the contrary “red shift” obtained in the Raman spectra. If the material is purely harmonic, their elastic moduli do not change with the addition of a small content of dopant. The degree to which the elastic moduli vary in the material will give a direct estimate of the degree of anharmonicity. The decreasing trend of shear and Young’s moduli of SnTe when doped with Ti/Zr/Mn, provides straightforward evidence of the rise in anharmonicity in the phonon modes of these Ti/Zr/Mn-doped SnTe compounds. The observed decrease in the speed of sound together with the reduction of elastic moduli in these doped SnTe compounds, are a direct consequence of the high anharmonic phonon modes arising from weakening of chemical bonds, that is, lattice softening effect. Such similar behavior was also reported for layered compounds with weak van der Waals bonding, such as Mg_3Sb_2 .^[101] In stark contrast, there are also compounds with high shear and Young’s moduli, such as $(\text{GeTe})_{17}\text{Sb}_2\text{Te}_3$, which were reported for lattice “hardening” effects.^[102] Mössbauer spectroscopy, which can enlighten more on the correlation between elastic moduli, the speed of sound, and the Debye temperature,^[103] makes a strong case for potential future work.

Table 4. Elastic properties calculated from density and speed of sound for SnTe-based samples.

Composition	v_L [m s ⁻¹]	v_T [m s ⁻¹]	Shear modulus, G [GPa]	Young’s modulus, Y [GPa]
SnTe	3451	1925	23.83	60.72
$\text{Sn}_{0.97}\text{Ti}_{0.03}\text{Te}$	3419	1881	22.82	58.56
$\text{Sn}_{0.98}\text{Zr}_{0.02}\text{Te}$	3402	1828	21.49	55.74
$\text{Sn}_{0.88}\text{Ti}_{0.03}\text{Mn}_{0.09}\text{Te}$	3398	1792	20.58	53.82
$\text{Sn}_{0.89}\text{Zr}_{0.02}\text{Mn}_{0.09}\text{Te}$	3352	1749	19.46	51.09

2.5.6. Visualization of Internal Strains

The lattice softening and lattice defects (dislocations, nano-precipitates), which locally change the phonon frequencies, will result in internal-strain fields in the material or vice-versa. Given the unique nature of the chemical bonding in these SnTe-based materials, they are more subtle to incorporating micro/nano-scale defects, and more specifically, the lattice strains. The internal strain of each sample (pristine SnTe, optimized Ti, Zr doped, and Ti-Mn and Zr-Mn codoped) was measured via XRD peak broadening by the Williamson–Hall method,^[104] which enables the determination of the average crystallite size (D) and micro-stain rate (ε) from powder XRD patterns by considering the evolution of the diffraction peak integral breadth (β in radian) as a function of $\sin(\theta)$ using the following equation:

$$\frac{\beta \times \cos(\theta)}{\lambda} = \frac{1}{D} + \frac{4\varepsilon \times \sin(\theta)}{\lambda} \quad (15)$$

Observed integral breadth was obtained by individually fitting the diffraction peak with a pseudo-Voigt profile function. The instrumental contribution (both Lorentzian and Gaussian contributions) was subtracted to the observed integral breadth to obtain the estimated intrinsic sample broadening, β . According to Equation (15), and in the case of an isotropic material, plotting $\beta \times \sin(\theta)/\lambda$ versus $2\varepsilon \times \sin(\theta)/\lambda$ gives a straight line which can be fitted using a linear function $y = ax + b$. Eventually, D and ε can be determined using the relations, $D = 1/b$ and $\varepsilon = a/2$. **Figure 18a** shows the Williamson–Hall plots for the optimized compositions, and **Table 5** gives the obtained values for the micro-strain rate. For all the compositions, the Williamson–Hall plot gives a crystallite size larger than 500 nm, which is considered as the highest resolution limit for this method when using a laboratory X-ray diffractometer.^[105] Also, it signifies that the only contribution to the broadening of the diffraction peaks comes from the lattice strains. A visual inspection of **Figure 18a** reveals that the plot for undoped, single-doped, and double-doped SnTe-samples mostly differ by their slopes' values. The slope of $\beta \times \sin(\theta)/\lambda$ versus $2\varepsilon \times \sin(\theta)/\lambda$ gives a direct measure of the magnitude of internal strain in the material. The slope, that is, micro-stain rate (ε) was indeed found to increase from 0.17% for undoped, to $\approx 0.30\%$ for Ti/Zr single-doped, and finally to $\approx 0.40\%$ for Ti-Mn/Zr-Mn double-doped SnTe (**Table 5**). The micro-strain rate obtained by XRD micro-structural analyses evidences the increase in internal strain-fields in SnTe with the substitution of Ti/Zr/Mn, and can be attributed to the lattice softening driven internal stresses, presence of several possible defects, such as dislocations, stacking faults, and twinning.^[105] To illustrate, the peak fits of SnTe and $\text{Sn}_{0.89}\text{Zr}_{0.02}\text{Mn}_{0.09}\text{Te}$ for (440) reflection are compared in **Figure 18b**. The $\text{Sn}_{0.89}\text{Zr}_{0.02}\text{Mn}_{0.09}\text{Te}$ sample with a high density of micro-strains shows a slight peak broadening effect/signs of peak shape asymmetry compared to pristine SnTe. Peak shape asymmetry is known to arise from extended lattice defects, including coherency strains and dislocations,^[56,105] and is linked to the reduction in phonon frequencies and speed of sound via the Grüneisen tensor.^[106] Indeed, in this case here, the presence of high density of internal strain-fields, which are potential phonon scattering centers, is reflected in the κ_{att} and

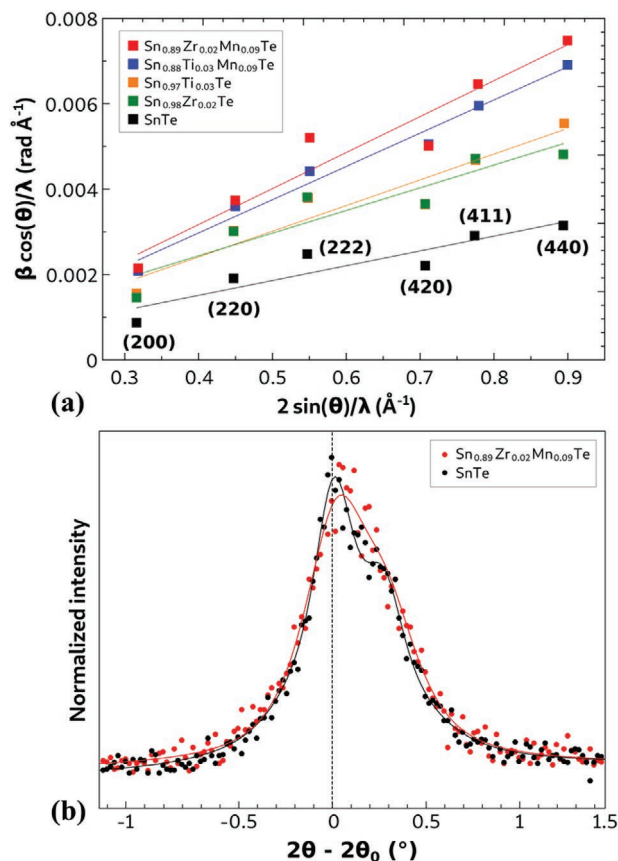


Figure 18. a) Williamson–Hall strain analysis of SnTe (black), $\text{Sn}_{0.98}\text{Zr}_{0.02}\text{Te}$ (green), $\text{Sn}_{0.97}\text{Ti}_{0.03}\text{Te}$ (orange), $\text{Sn}_{0.88}\text{Ti}_{0.03}\text{Mn}_{0.09}\text{Te}$ (blue) and $\text{Sn}_{0.89}\text{Zr}_{0.02}\text{Mn}_{0.09}\text{Te}$ (red). β is the integral breadth (peak area/height) of a diffraction peak at θ . The slope of this Williamson–Hall plot for each sample is proportional to the average internal strain in that sample, b) a representative peak fit of $\text{Sn}_{0.89}\text{Zr}_{0.02}\text{Mn}_{0.09}\text{Te}$ (red) in comparison with pristine SnTe (black) for the (440) reflection showing signs of peak shape asymmetry/peak broadening effect due to the presence of high density of internal strains.

measured v_s values of Ti/Zr/Mn-doped SnTe, that is, the trend of the micro-stain rate (ε) is consistent with the trend of the reduction in the speed of sound and in thermal conductivity, when single dopant (Ti/Zr) or double (Ti-Mn/Zr-Mn) dopants are systematically introduced into the SnTe, as depicted in **Figure 19a,b**. The phonon transport relies on a change in either atomic mass M or force constant F , and materials with

Table 5. Micro-strain rate for SnTe-based compounds determined from Williamson–Hall analysis^[104] of XRD data. The crystallite size in all the cases were found be larger than 500 nm.

Composition	Micro-strain [ε]
SnTe	0.17%
$\text{Sn}_{0.97}\text{Ti}_{0.03}\text{Te}$	0.30%
$\text{Sn}_{0.98}\text{Zr}_{0.02}\text{Te}$	0.27%
$\text{Sn}_{0.88}\text{Ti}_{0.03}\text{Mn}_{0.09}\text{Te}$	0.39%
$\text{Sn}_{0.89}\text{Zr}_{0.02}\text{Mn}_{0.09}\text{Te}$	0.42%

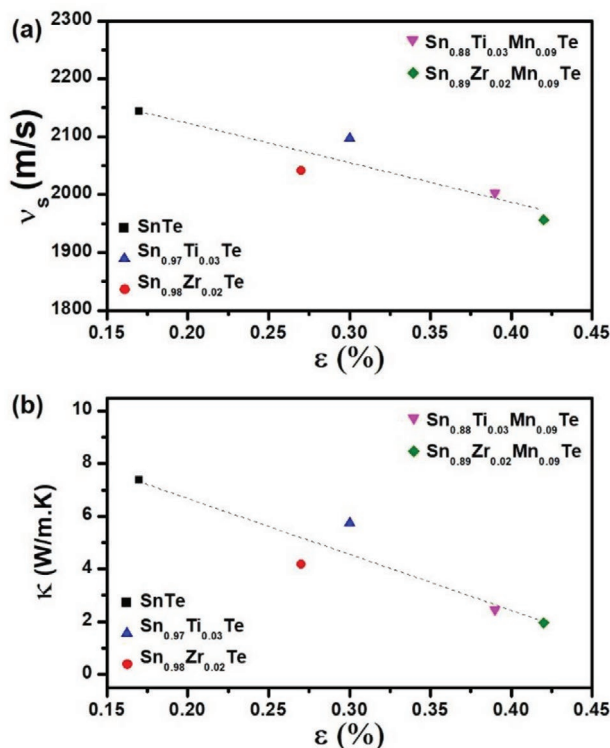


Figure 19. a) The speed of sound (v_s) measured using pulse-echo ultrasound technique versus the amount of internal strain estimated using the Williamson–Hall analysis of XRD patterns of SnTe-based samples follows the $v_s = v_{s,0} (1 - \gamma_{inj} \epsilon)$ relation, b) the evolution of thermal conductivity as a function of internal strain in the SnTe-based materials. The slight deviation in the linearity trend for single doped Ti/Zr systems is due to the differences in their estimated strain, which is well within the acceptable error limits. From (a) and (b), the decrease in the speed of sound and the thermal conductivity can be directly correlated (linear) to the increase in internal strain in these SnTe-samples.

a large M and/or small F tend to show a low lattice thermal conductivity. The decrease in sound velocity and increase in lattice strains (Figure 19a) clearly points at a decrease in force constant (weak chemical bonds) with Ti/Zr/Mn substitution in SnTe, as $v_s \propto (F/M)^{1/2}$. Such raise in lattice anharmonicity can in fact lead to fluctuations (broadening) in angular frequency (ω , also known as phonon dispersion that fundamentally governs the phonon transport) through a fluctuated effective force constant F at a given wave vector (k).^[107] This linear decrease of phonon frequency (ω) and/or the speed of sound (v_s) with the internal strain-field (ϵ) in a given material system is consistent with the following equation:^[56,106]

$$v_s = v_{s,0}(1 - \gamma_{inj}\epsilon) \quad (16)$$

where $v_{s,0}$ is the speed of sound at zero strain, and γ_{inj} is the Grüneisen tensor. The theoretical aspects of the impact of mechanical strain on the thermoelectric properties have been elucidated in the past for materials such as silicon, Bi_2Te_3 and Sb_2Te_3 .^[108,109] The correlation of linear decrease of the speed of sound (Figure 19a) and thermal conductivity (Figure 19b) with the increase in internal strain in these SnTe-based materials

further corroborates the aforementioned reasons and evidences given in the previous paragraphs. It must be noted that to correct the effect of elastic anisotropy and to correlate the crystallite size from XRD and the grain size from TEM, X-ray line profile analysis using a “modified” Williamson–Hall method (mWH)^[110,111] might be necessary.

2.6. Comparison of the Average Figure of Merit and Thermoelectric Efficiency (with $T \leq 723$ K and $\Delta T = 400$ K) for SnTe-Based Compounds

Because of the simultaneous enhancement in the electrical transport properties and significant suppression of the thermal transport properties due to the combination of reasons/factors stated in the previous sections, the maximum figure of merit (zT_{\max}) at mid-temperature ranges for the Ti/Zr single doped and Ti-Mn/Zr-Mn codoped SnTe systems are mostly comparable with some of the best reported SnTe-based materials in that temperature range (≤ 723 K),^[27,28,40,50,59,65,79,112–114] as shown in Figure 20a. For the codoped cases (Ti-Mn/Zr-Mn), the $zT_{\max} \approx 0.7$ is attained in the mid-temperature ranges. Of course, there certainly are several other SnTe-based materials that exhibit $zT_{\max} > 1$, but it must be noted that the peak performance in those materials occurs only at high-temperature ranges (823–873 K, or higher),^[24,28,54,94] thus limiting their practicality in an application. It is one of the prime reasons why the comparison is kept within the more realistic temperature domain (≤ 723 K) in this work. More importantly, the results are reproducible and consistent during the heating and cooling cycles (Figure S2, Supporting Information). The calculations of the average dimensionless figure of merit zT_{ave} (also referred as device zT or zT_{device}) were done by integrating the area under the temperature-dependent zT curves according to Equation (17):^[57]

$$zT_{\text{ave}} = \frac{1}{T_h - T_c} \int_{T_c}^{T_h} zT \cdot dT \quad (17)$$

The maximum efficiency (η) of a single thermoelectric leg is given by the following equation:^[57,115]

$$\eta = \frac{T_h - T_c}{T_h} \left[\frac{\sqrt{1 + zT_{\text{ave}}} - 1}{\sqrt{1 + zT_{\text{ave}}} + T_c/T_h} \right] \quad (18)$$

The importance of improved performance (both electrical and thermal transport) right from room temperature to mid-temperature ranges for these Ti/Zr doped SnTe materials are reflected in their zT_{ave} or zT_{device} (Figure 20b). For a comparison, Mg-doped SnTe^[40] and V-doped SnTe^[50] exhibit much higher zT_{\max} at higher temperature regions ($zT_{\max} > 1$ at $T > 823$ K) and fairly similar zT_{\max} at 723 K as that of Ti/Zr doped SnTe materials that are presented in this work (Figure 20a). But however, as the overall performance of Ti/Zr-doped SnTe at each temperature interval (right from room temperature to mid-temperature ranges) is superior, they exhibit higher zT_{device} than the Mg/V doped SnTe, in spite of their superior zT_{\max} values (Figure 20b). The situation remains the same with codoped SnTe, that is, for instance, the Bi-Pb codoped SnTe exhibits an

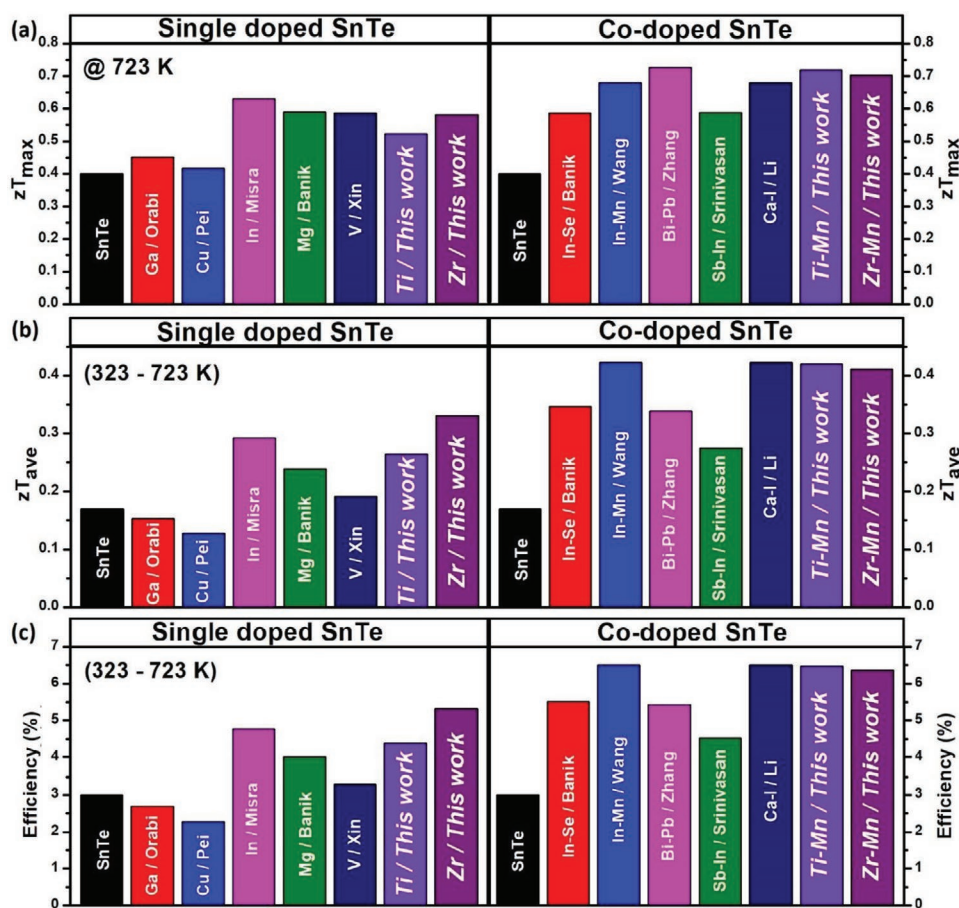


Figure 20. Thermoelectric performance of optimized Ti//Zr doped SnTe in this work is compared with other reported SnTe dopants like Ga,^[79] Cu,^[113] In,^[59] Mg,^[40] V,^[50] and the Ti-Mn/Zr-Mn codoped SnTe in this work is compared with other reported SnTe codopants such as In-Se,^[114] In-Mn,^[27] Bi-Pb,^[28] Sb-In,^[112] Ca-I.^[65] a) Maximum/peak figure of merit, zT_{\max} (at 723 K) for SnTe-based materials, b) average figure of merit, zT_{ave} (or zT_{device}) for SnTe-based materials, and c) maximum efficiency, η , of a single thermoelectric leg. The comparison of zT_{ave} , and η are made at a finite temperature difference, $\Delta T = T_h - T_c = 323 - 723 \text{ K} = 400 \text{ K}$.

attractive zT_{\max} at a higher temperature ($zT_{\max} > 1$ at 850 K),^[28] but the overall performance throughout the whole temperature range is not so impressive, thus exhibiting lower zT_{device} than Ti-Mn/Zr-Mn codoped SnTe materials that are reported here (Figure 20b). From a practical point of view, it is not the maximum zT (zT_{\max}), but it is the average zT (zT_{ave}) value that governs the overall efficiency of a TE module, as referred in Equation (18). By setting the hot side temperature as 723 K and the cold side temperature as 323 K, the efficiency of a single TE leg is estimated based on Equation (18), the results of which are presented in Figure 20c. It clearly shows that the zT_{device} of a given material is directly proportional to the efficiency, η . Literature reports have predicted $\eta > 10\%$ for some SnTe-based materials, but with a much higher temperature gradient of $\geq 600 \text{ K}$ ($T_c = 300 \text{ K}$, $T_h = 900\text{--}923 \text{ K}$).^[28,54] It is quintessential for a real-time commercial application to have a thermoelectric power generator operating at a relatively lower ΔT . For a $\Delta T \leq 400 \text{ K}$, Zr-SnTe (single doped) and Ti-Mn/Zr-Mn-SnTe (codoped) compounds that are presented in this work significantly prevails over most of the previously reported single/codoped SnTe analogues and competes (comparable) with some of the best reported state-of-the-art counterparts at this operating window

of $T_c = 323 \text{ K}$, $T_h = 723 \text{ K}$ (Figure 20c). This strongly endorses the fact that it is feasible to realize high thermoelectric efficiency without the need for a striking zT_{\max} , and reiterates that the focus should rather be on improving the overall performance in the practically workable temperature range (high zT_{ave} with a small ΔT).

3. Conclusion

High-dense, pure and homogeneous samples of Ti-doped and Zr-doped SnTe compounds were synthesized via the melt-processing and SPS compaction method. Through the measurement of electrical and thermal transport properties, the optimized compositions were found to be $\text{Sn}_{0.97}\text{Ti}_{0.03}\text{Te}$ and $\text{Sn}_{0.98}\text{Zr}_{0.02}\text{Te}$, to which Mn was codoped to form the Ti-Mn and Zr-Mn codoped SnTe compounds. The optimized single (Ti/Zr) doping and codoping (Ti-Mn/Zr-Mn) enabled an improvement in the electrical transport of SnTe, thanks to an amalgamation of factors, such as i) bolstering of weighted mobility by striking the suitable trade-off between the effective mass, carrier concentration and carrier mobility, ii) bringing

in the mixed carrier scattering mechanisms, iii) manipulating the electronic band structure by increasing the density of states (with Ti), engineering the carrier-pockets to raise the effective mass (with Zr), and corrugated flat-bands yielding multiple Fermi-surfaces, besides opening up the forbidden energy gap and reducing the energy separation between the light and heavy hole valence bands (with codoping), and iv) feasible interaction between the carriers and magnetic moments (with Mn-codoping to Ti/Zr), and more importantly (v) these transition dopants (Ti/Zr/Mn), when added to SnTe, softened the chemical bonds, which resulted in high anharmonicity with a decrease in the elastic moduli (Shear and Young's modulus) and an increase in the internal strain-fields that simultaneously changed the phonon group velocity (speed of sound) and induced phonon scattering. The synergistic effect of lattice softening and phonon scattering markedly suppressed the thermal transport in Ti/Zr-Mn doped SnTe compounds. The commingled effects of enhanced electrical transport and suppressed thermal transport over the entire spectrum of low-mid temperature ranges (323–723 K), enabled the Zr-doped and Ti/Zr-Mn codoped SnTe to outperform/compete with some of the best reported SnTe analogues in terms of device/average figure of merit and thermoelectric efficiency for an impressively lower $\Delta T \approx 400$ K.

From a broader context, besides the thermoelectric aspects of SnTe, this work also strives to enlighten the importance of experimental weighted mobility (rather than the conventional power factor) as an effective descriptor to elucidate the electrical transport properties and excavates/opens up the discussion of applying the Heikes' equation to qualitatively compare the trend of charge carriers for a given thermoelectric material system.

4. Experimental Section

Reagents: Sn (shot, High Purity Chemicals, 99.999%), Te (shot, Rare Metallic, 99.999%), Ti (sponge, Aldrich, 99.5%), Zr (sponge, Aldrich, >99%), and Mn (flake, Wako, 99.95%) were used for synthesis without any further purification.

Synthesis: The SnTe-based samples were synthesized via a vacuum-sealed tube melt processing route. It must be noted that, just like in many other SnTe-based materials that are reported so far, the self-compensated $\text{Sn}_{1.03-x}\text{M}_x\text{Te}$ ($M = \text{dopant}$) nominal composition was adopted here to reach the actual stoichiometry and to optimize their charge carrier concentration,^[37,40,59,64,79,86] that is, to compensate for the inherent nature of SnTe to have Sn vacancies (Sn_{1-x}Te). From the crystallographic point of view, it was not possible to have excess Sn in the structure (SnTe). Therefore, the compositions are referred in stoichiometric terms (SnTe or $\text{Sn}_{1-x}\text{M}_x\text{Te}$) throughout this paper, rather than the nominal $\text{Sn}_{1.03}\text{Te}$ or $\text{Sn}_{1.03-x}\text{M}_x\text{Te}$. Appropriate amounts of the starting elements were placed into a quartz tube and evacuated until ≈ 2 μbar . The evacuated tubes were then sealed and placed in a controllable temperature furnace, where they were slowly heated up to 1173 K in about 8 h and held at that temperature for about 8 h before gently cooling down to room temperature. The obtained ingots were crushed and grinded into fine powders (<200 μm) using pestle and mortar. The crushed powders were then densified by Spark Plasma Sintering (SPS-1080—SPS Syntex Inc.) into discs of 10 mm diameter. The sintering process was done under partial Argon atmosphere at 773 K for 10 min (holding time) with a heating rate ≈ 75 K h^{-1} with an axial pressure of ≈ 65 MPa. After sintering, the obtained consolidated samples were cleaned, checked for density (Archimedes' method), and processed

into the corresponding size and shape for various transport property measurements.

Powder X-Ray Diffraction: Powder X-ray diffraction (XRD) patterns were measured at room temperature using a Rigaku Smart Lab 3 diffractometer (Cu radiation, $\lambda_{\text{CuK}\alpha 1} = 1.5418$ \AA , and $\lambda_{\text{CuK}\alpha 2} = 1.5444$ \AA , $\lambda_{\text{CuK}\alpha 2}/\lambda_{\text{CuK}\alpha 1}$ ratio of 0.5) with a step size of 0.02° and a scan speed of 2°min^{-1} . Le Bail refinements were performed using the MAUD software.^[116] The shape of the diffraction peaks was modeled using a Thompson Cox-Hastings pseudo-Voigt function.^[117] The refined parameters were the zero-point shift, peak shape parameters, and the lattice constant. The instrumental resolution of the diffractometer was determined by measuring a Si 640f-NIST reference sample ($a = 5.43114(8)$ \AA). The instrumental contribution to the diffraction peak broadening was subtracted to the observed integral breadth to provide an estimated intrinsic sample broadening (β in radian). For selected samples, the crystallite size (D) and micro-strain (ϵ) were derived from the Williamson–Hall plot.^[104]

Microscopic Analysis: The samples' microstructural features were analyzed on the fractured surface of the sintered samples using a Hitachi SU-8000 Scanning Electron Microscope (SEM), and the compositional analysis on the polished flat surface using energy dispersive spectroscopy (EDX).

Electrical and Thermal Transport Measurements: The Seebeck coefficient (S) and electrical conductivity (σ) were measured simultaneously on samples of dimension $\approx 2 \times 2 \times 9$ mm^3 using ZEM2 (Advance Riko Inc.) under the partial pressure of He. LFA 467 Hyperflash (Netzsch) was used to measure the thermal diffusivity (D) and specific heat (C_p). The measurements were made on disc-shaped samples of 10 mm diameter and ≈ 2 mm thickness. The temperature-dependent C_p derived using the standard/reference sample (Pyroceram-9060) was found to be in agreement with the C_p from the Dulong-Petit relation ($C_p = 3R/M$, where R is the ideal gas constant and M is the molar mass). The total thermal conductivity (κ) was calculated using the following equation:

$$\kappa = DC_p \rho \quad (19)$$

where ρ is the density obtained via Archimedes' method. It must be noted that the density of these SPS processed SnTe-based samples was $\geq 99\%$ of the theoretical density. The electronic and lattice contribution to the thermal conductivity, κ_e and κ_{latt} , respectively, were also calculated. κ_e is calculated using the Wiedemann-Franz law, as given below,

$$\kappa_e = L\sigma T \quad (20)$$

where L is the Lorenz number calculated using the condensed version of the single parabolic band model with acoustic phonon scattering (SPB-APS),^[118–120] as given in the following relation,

$$L = 1.5 + \exp\left[-\frac{|S|}{116}\right] \quad (21)$$

where the Seebeck coefficient, S is in $\mu\text{V K}^{-1}$, and L is in $10^{-8} \text{W } \Omega \text{K}^{-2}$.

For the electrical transport property measurements, the uncertainty in the values of the results was $\approx 5\%$, while it was $\approx 7\%$ for thermal transport and $\approx 12\%$ for the overall zT .^[121,122] For the purpose of better readability, the error bars are not shown in the figures.

Sound Velocity Measurements: The pulse-echo method was used to measure the speed of sound in the SnTe-based materials. The measurements were made on disc-shaped samples of 10 mm diameter and ≈ 2 mm thickness. The samples were coupled to a piezoelectric transducer with a small amount of lubricant (grease). The transducer receives and measures the echoed ultrasound reflections by acting as a detector when it initially sends a stress-wave pulse into the sample. By maximizing the cross-correlation of the two reflections, the time delay (t_d) was estimated, and the sound velocity in a specific direction (v) is calculated using the following relation,^[24,94]

$$v = \frac{2d}{t_d} \quad (22)$$

where d is the thickness of the sample. The sound velocity was measured along both longitudinal (v_L) and transverse (v_T) directions using 10 MHz longitudinal and transverse transducers (Ultrasonic Engineering Co. Ltd.—10K4NPS5, 10Z5SNPS4, respectively). To record the waveforms, a Tektronix (TBS 1072B) oscilloscope was used. To minimize the percentage of error/standard deviation, several waveforms were collected at various pulse/receiver gain and damping levels, and the resulting speed of sound results was averaged.

Raman Spectroscopy: The vibrational modes of the different SnTe compounds were determined by the RAMANplus spectrometer (Nanophoton, Osaka, Japan) at a single excitation wavelength of 532 nm. The Raman spectra were obtained in the frequency range of 19.5–517 cm^{-1} using a laser power of 0.88 mW, a grating of 2400 g mm^{-1} , and a slit width of 50 mm.

Computational Details: In order to understand the electronic transport properties, first-principles calculations based on Density Functional Theory (DFT) were performed to compute the density of states (DOS) and electronic band structures of pristine and transition metal (Ti, Zr, Mn) doped SnTe systems. In the present case, self-consistency field (SCF) and electronic structure calculations were carried out by using the DFT tools established on linearized full potential augmented plane-wave (lapw) and local orbitals (lo) method, developed into the WIEN2k code.^[123] The exchange-correlation interaction was described within the generalized gradient approximation (GGA) using the parametrization of the Perdew–Burke–Ernzerhof (PBE) functional.^[124,125] All SCF calculations were carried out using the experimental lattice parameters obtained from the structural refinements. The plane wave cutoff parameters ($R_{\text{MT}}K_{\text{max}} = 7$), and expansion of radial wave function, which safely maintain the non-overlapping of the muffin tin spheres, were set to be $l_{\text{max}} = 12$. Total energy convergence was achieved with a Brillouin zone (BZ) integration mesh of 500 k -points. Supercells of size $2 \times 2 \times 2$ consisting of 64 atoms for pristine, Ti-doped, and Ti-Mn codoped SnTe systems (i.e., $\text{Sn}_{32}\text{Te}_{32}$, $\text{Sn}_{31}\text{TiTe}_{32}$, and $\text{Sn}_{28}\text{TiMn}_3\text{Te}_{32}$ models), and $4 \times 4 \times 4$ consisting of 128 atoms for Zr-doped and Zr-Mn codoped SnTe systems (i.e., $\text{Sn}_{63}\text{ZrTe}_{64}$, and $\text{Sn}_{57}\text{Zr}_1\text{Mn}_6\text{Te}_{64}$) were considered, in a way such that they closely represent the experimental compositions. For the purpose of simplicity, though there are some magnetic interactions in the doped samples, the magnetic contribution was not considered in these computations.

Supporting Information

Supporting Information is available from the Wiley Online Library or from the author.

Acknowledgements

A.R.M. and B.S. contributed equally to this work. A.R.M. acknowledges NIMS-ICGP program for the Indonesia–Japan mobility grant. B.S. acknowledges the Japan Society for the Promotion of Science (JSPS) for the postdoctoral fellowship (P19720). B.S. also thanks Dr. Clarisse Bloyet and Dr. Naoki Sato from NIMS for their kind assistance with Raman and sound velocity measurements, respectively, and Prof. Jean-François Halet for his constant support. S.S. thanks Prof. Tsunehiro Takeuchi (Toyota Tech. Inst.) for providing the access to the computational facilities for DFT. T.M. acknowledges the funding from JSPS KAKENHI 19F19720, JP16H06441, and JST-Mirai JPMJMI19A1. S.L.T. and D.B. acknowledge ANR for the funding (ANR-18-CE05-0037). Philipp Sauerschnig, Raju Chetty, Cédric Bourgès, Wenhao Zhang and Christopher Hassam are thanked for their friendships.

Conflict of Interest

The authors declare no conflict of interest.

Data Availability Statement

Research data are not shared.

Keywords

chemical bond weakening, Heikes' equation, SnTe, thermoelectrics

Received: April 8, 2021

Revised: May 26, 2021

Published online: June 9, 2021

- [1] L. E. Bell, *Science* **2008**, 321, 1457.
- [2] J. He, T. M. Tritt, *Science* **2017**, 357, eaak9997.
- [3] M. T. Dunham, T. J. Hendricks, K. E. Goodson, in *Adv. Heat Transf.* (Eds: E. M. Sparrow, J. P. Abraham, J. M. Gorman, W. J. Minkowycz), Elsevier, New York **2019**, p. 299.
- [4] I. Petsagkourakis, K. Tybrandt, X. Crispin, I. Ohkubo, N. Satoh, T. Mori, *Sci. Technol. Adv. Mater.* **2018**, 19, 836.
- [5] B. Srinivasan, S. Cui, C. Prestipino, A. Gellé, C. Boussard-Pledel, S. Ababou-Girard, A. Trapananti, B. Bureau, S. Di Matteo, *J. Phys. Chem. C* **2017**, 121, 14045.
- [6] N. Nandihalli, C.-J. Liu, T. Mori, *Nano Energy* **2020**, 78, 105186.
- [7] T. Zhang, Z. Wang, B. Srinivasan, Z. Wang, J. Zhang, K. Li, C. Boussard-Pledel, J. Troles, B. Bureau, L. Wei, *ACS Appl. Mater. Interfaces* **2019**, 11, 2441.
- [8] B. Srinivasan, *Ph.D. Thesis*, Université Rennes, **2018**.
- [9] J. R. Sootsman, D. Y. Chung, M. G. Kanatzidis, *Angew. Chem., Int. Ed.* **2009**, 48, 8616.
- [10] G. J. Snyder, E. S. Toberer, *Nat. Mater.* **2008**, 7, 105.
- [11] B. Srinivasan, S. L. Tonquesse, A. Gellé, C. Bourgès, L. Monier, I. Ohkubo, J.-F. Halet, D. Berthebaud, T. Mori, *J. Mater. Chem. A* **2020**, 8, 19805.
- [12] A. Pakdel, Q. Guo, V. Nicolosi, T. Mori, *J. Mater. Chem. A* **2018**, 6, 21341.
- [13] D. V. M. Repaka, A. Suwardi, P. Kumar, in *Energy Sav. Coat. Mater.* (Eds: G. K. Dalapati, M. Sharma), Elsevier, New York **2020**, p. 183.
- [14] B. Srinivasan, A. Gellé, F. Gucci, C. Boussard-Pledel, B. Fontaine, R. Gautier, J.-F. Halet, M. J. Reece, B. Bureau, *Inorg. Chem. Front.* **2019**, 6, 63.
- [15] Z. Zheng, X. Su, R. Deng, C. Stoumpos, H. Xie, W. Liu, Y. Yan, S. Hao, C. Uher, C. Wolverton, M. G. Kanatzidis, X. Tang, *J. Am. Chem. Soc.* **2018**, 140, 2673.
- [16] D. Narducci, E. Selezneva, G. Cerofolini, S. Frabboni, G. Ottaviani, *J. Solid State Chem.* **2012**, 193, 19.
- [17] A. Suwardi, L. Hu, X. Wang, X. Y. Tan, D. V. M. Repaka, L.-M. Wong, X. Ni, W. H. Liew, S. H. Lim, Q. Yan, J. Xu, Y. Zheng, K. Hippalgaonkar, *ACS Appl. Mater. Interfaces* **2020**, 12, 9150.
- [18] B. Srinivasan, A. Gellé, J.-F. Halet, C. Boussard-Pledel, B. Bureau, *Materials* **2018**, 11, 2237.
- [19] M. G. Kanatzidis, *Chem. Mater.* **2010**, 22, 648.
- [20] R. V. R. Virtudazo, B. Srinivasan, Q. Guo, R. Wu, T. Takei, Y. Shimasaki, H. Wada, K. Kuroda, S. Bernik, T. Mori, *Inorg. Chem. Front.* **2020**, 7, 4118.
- [21] A. U. Khan, K. Kobayashi, D.-M. Tang, Y. Yamauchi, K. Hasegawa, M. Mitome, Y. Xue, B. Jiang, K. Tsuchiya, D. Golberg, Y. Bando, T. Mori, *Nano Energy* **2017**, 31, 152.
- [22] W. Zhang, N. Sato, K. Tobita, K. Kimura, T. Mori, *Chem. Mater.* **2020**, 32, 5335.
- [23] C. Bourgès, B. Srinivasan, B. Fontaine, P. Sauerschnig, A. Minard, J.-F. Halet, Y. Miyazaki, D. Berthebaud, T. Mori, *J. Mater. Chem. C* **2020**, 8, 16368.

- [24] T. J. Slade, K. Pal, J. A. Grovogui, T. P. Bailey, J. Male, J. F. Khoury, X. Zhou, D. Y. Chung, G. J. Snyder, C. Uher, V. P. Dravid, C. Wolverton, M. G. Kanatzidis, *J. Am. Chem. Soc.* **2020**, *142*, 12524.
- [25] F. Gucci, T. G. Saunders, B. Srinivasan, F. Cheviré, D. A. Ferlucchio, J.-W. G. Bos, M. J. Reece, *J. Alloys Compd.* **2020**, *837*, 155058.
- [26] R. Moshwan, L. Yang, J. Zou, Z.-G. Chen, *Adv. Funct. Mater.* **2017**, *27*, 1703278.
- [27] L. Wang, X. Tan, G. Liu, J. Xu, H. Shao, B. Yu, H. Jiang, S. Yue, J. Jiang, *ACS Energy Lett.* **2017**, *2*, 1203.
- [28] X. Zhang, D. Wang, H. Wu, M. Yin, Y. Pei, S. Gong, L. Huang, S. J. Pennycook, J. He, L.-D. Zhao, *Energy Environ. Sci.* **2017**, *10*, 2420.
- [29] H. Deng, X. Lou, W. Lu, J. Zhang, D. Li, S. Li, Q. Zhang, X. Zhang, X. Chen, D. Zhang, Y. Zhang, G. Tang, *Nano Energy* **2021**, *81*, 105649.
- [30] F. Guo, B. Cui, M. Guo, J. Wang, J. Cao, W. Cai, J. Sui, *Mater. Today Phys.* **2019**, *11*, 100156.
- [31] Z. Chen, X. Guo, F. Zhang, Q. Shi, M. Tang, R. Ang, *J. Mater. Chem. A* **2020**, *8*, 16790.
- [32] B. Srinivasan, B. Fontaine, F. Gucci, V. Dorcet, T. G. Saunders, M. Yu, F. Cheviré, C. Boussard-Pledel, J.-F. Halet, R. Gautier, M. J. Reece, B. Bureau, *Inorg. Chem.* **2018**, *57*, 12976.
- [33] C. W. Li, O. Hellman, J. Ma, A. F. May, H. B. Cao, X. Chen, A. D. Christianson, G. Ehlers, D. J. Singh, B. C. Sales, O. Delaire, *Phys. Rev. Lett.* **2014**, *112*, 175501.
- [34] S. Lee, K. Esfarjani, T. Luo, J. Zhou, Z. Tian, G. Chen, *Nat. Commun.* **2014**, *5*, 3525.
- [35] B. Srinivasan, F. Gucci, C. Boussard-Pledel, F. Cheviré, M. J. Reece, S. Tricot, L. Calvez, B. Bureau, *J. Alloys Compd.* **2017**, *729*, 198.
- [36] G. Tan, F. Shi, J. W. Doak, H. Sun, L.-D. Zhao, P. Wang, C. Uher, C. Wolverton, V. P. Dravid, M. G. Kanatzidis, *Energy Environ. Sci.* **2014**, *8*, 267.
- [37] R. Al Rahal Al Orabi, N. A. Mecholsky, J. Hwang, W. Kim, J.-S. Rhyee, D. Wee, M. Fornari, *Chem. Mater.* **2016**, *28*, 376.
- [38] Q. Zhang, B. Liao, Y. Lan, K. Lukas, W. Liu, K. Esfarjani, C. Opeil, D. Broido, G. Chen, Z. Ren, *Proc. Natl. Acad. Sci. USA* **2013**, *110*, 13261.
- [39] Z. Chen, X. Guo, J. Tang, F. Xiong, W. Li, Y. Chen, R. Ang, *ACS Appl. Mater. Interfaces* **2019**, *11*, 26093.
- [40] A. Banik, U. S. Shenoy, S. Anand, U. V. Waghmare, K. Biswas, *Chem. Mater.* **2015**, *27*, 581.
- [41] G. Tan, F. Shi, S. Hao, H. Chi, T. P. Bailey, L.-D. Zhao, C. Uher, C. Wolverton, V. P. Dravid, M. G. Kanatzidis, *J. Am. Chem. Soc.* **2015**, *137*, 11507.
- [42] A. Banik, U. S. Shenoy, S. Saha, U. V. Waghmare, K. Biswas, *J. Am. Chem. Soc.* **2016**, *138*, 13068.
- [43] X. Tan, X. Tan, G. Liu, J. Xu, H. Shao, H. Hu, M. Jin, H. Jiang, J. Jiang, *J. Mater. Chem. C* **2017**, *5*, 7504.
- [44] R. Moshwan, W.-D. Liu, X.-L. Shi, Y.-P. Wang, J. Zou, Z.-G. Chen, *Nano Energy* **2019**, *65*, 104056.
- [45] Z. Li, Y. Chen, J.-F. Li, H. Chen, L. Wang, S. Zheng, G. Lu, *Nano Energy* **2016**, *28*, 78.
- [46] R. D. Schmidt, E. D. Case, J. E. Ni, R. M. Trejo, E. Lara-Curzio, R. J. Korkosz, M. G. Kanatzidis, *J. Mater. Sci.* **2013**, *48*, 8244.
- [47] Z. Chen, Q. Sun, F. Zhang, J. Mao, Y. Chen, M. Li, Z.-G. Chen, R. Ang, *Mater. Today Phys.* **2021**, *17*, 100340.
- [48] X. Li, J. Liu, S. Li, J. Zhang, D. Li, R. Xu, Q. Zhang, X. Zhang, B. Xu, Y. Zhang, F. Xu, G. Tang, *Nano Energy* **2020**, *67*, 104261.
- [49] T. Hussain, X. Li, M. H. Danish, M. U. Rehman, J. Zhang, D. Li, G. Chen, G. Tang, *Nano Energy* **2020**, *73*, 104832.
- [50] J. Xin, S. Li, J. Yang, A. Basit, Q. Long, S. Li, Q. Jiang, T. Xu, B. Xiao, *Nano Energy* **2020**, *67*, 104292.
- [51] R. Moshwan, X.-L. Shi, W.-D. Liu, Y. Wang, S. Xu, J. Zou, Z.-G. Chen, *ACS Appl. Energy Mater.* **2019**, *2*, 2965.
- [52] M. Hong, Y. Wang, S. Xu, X. Shi, L. Chen, J. Zou, Z.-G. Chen, *Nano Energy* **2019**, *60*, 1.
- [53] F. Guo, B. Cui, Y. Liu, X. Meng, J. Cao, Y. Zhang, R. He, W. Liu, H. Wu, S. J. Pennycook, W. Cai, J. Sui, *Small* **2018**, *14*, 1802615.
- [54] H. Wang, J. Hwang, C. Zhang, T. Wang, W. Su, H. Kim, J. Kim, J. Zhai, X. Wang, H. Park, W. Kim, C. Wang, *J. Mater. Chem. A* **2017**, *5*, 14165.
- [55] G. J. Snyder, A. H. Snyder, M. Wood, R. Gurunathan, B. H. Snyder, C. Niu, *Adv. Mater.* **2020**, *32*, 2001537.
- [56] R. Hanus, M. T. Agne, A. J. E. Rettie, Z. Chen, G. Tan, D. Y. Chung, M. G. Kanatzidis, Y. Pei, P. W. Voorhees, G. J. Snyder, *Adv. Mater.* **2019**, *31*, 1900108.
- [57] G. J. Snyder, A. H. Snyder, *Energy Environ. Sci.* **2017**, *10*, 2280.
- [58] H. Taguchi, M. Sonoda, M. Nagao, *J. Solid State Chem.* **1998**, *137*, 82.
- [59] S. Misra, B. Wiendlocha, J. Tobola, F. Fesquet, A. Dauscher, B. Lenoir, C. Candolfi, *J. Mater. Chem. C* **2019**, *8*, 977.
- [60] D. Ibrahim, C. Candolfi, S. Migot, J. Ghanbaja, A. Dauscher, G. L. e Caër, B. Malaman, C. Semprimoschnig, B. Lenoir, *Phys. Rev. Mater.* **2019**, *3*, 085404.
- [61] S. Le Tonquesse, M. Pasturel, V. Demange, A. Tayal, P. L. Solari, C. Prestipino, *J. Nucl. Mater.* **2019**, *526*, 151772.
- [62] M. Aminzare, Y.-C. Tseng, A. Ramakrishnan, K.-H. Chen, Y. Mozharivskiy, *Sustainable Energy Fuels* **2018**, *3*, 251.
- [63] A. Banik, B. Vishal, S. Perumal, R. Datta, K. Biswas, *Energy Environ. Sci.* **2016**, *9*, 2011.
- [64] Z. Ma, J. Lei, D. Zhang, C. Wang, J. Wang, Z. Cheng, Y. Wang, *ACS Appl. Mater. Interfaces* **2019**, *11*, 33792.
- [65] S. Li, J. Yang, J. Xin, Q. Jiang, Z. Zhou, H. Hu, B. Sun, A. Basit, X. Li, *ACS Appl. Energy Mater.* **2019**, *2*, 1997.
- [66] M. Cutler, J. F. Leavy, R. L. Fitzpatrick, *Phys. Rev.* **1964**, *133*, A1143.
- [67] D. Srivastava, C. Norman, F. Azough, D. Ekren, K. Chen, M. J. Reece, I. A. Kinloch, R. Freer, *J. Mater. Chem. A* **2019**, *7*, 24602.
- [68] D. Srivastava, C. Norman, F. Azough, M. C. Schäfer, E. Guilmeau, D. Kepaptsoglou, Q. M. Ramasse, G. Nicotra, R. Freer, *Phys. Chem. Chem. Phys.* **2016**, *18*, 26475.
- [69] J. J. Kuo, S. D. Kang, K. Imasato, H. Tamaki, S. Ohno, T. Kanno, G. J. Snyder, *Energy Environ. Sci.* **2018**, *11*, 429.
- [70] H. Xie, H. Wang, C. Fu, Y. Liu, G. J. Snyder, X. Zhao, T. Zhu, *Sci. Rep.* **2014**, *4*, 6888.
- [71] H. Wang, Y. Pei, A. D. LaLonde, G. J. Snyder, in *Thermoelectr. Nanomater. Mater. Des. Appl.* (Eds: K. Koumoto, T. Mori), Springer, Berlin **2013**, p. 3.
- [72] Y. Katsura, M. Kumagai, T. Kodani, M. Kaneshige, Y. Ando, S. Gunji, Y. Imai, H. Ouchi, K. Tobita, K. Kimura, K. Tsuda, *Sci. Technol. Adv. Mater.* **2019**, *20*, 511.
- [73] Z. Liu, J. Mao, S. Peng, B. Zhou, W. Gao, J. Sui, Y. Pei, Z. Ren, *Mater. Today Phys.* **2017**, *2*, 54.
- [74] T. Wang, H. Wang, W. Su, J. Zhai, G. Yakovleva, X. Wang, T. Chen, A. Romanenko, C. Wang, *J. Mater. Chem. C* **2020**, *8*, 7393.
- [75] J. Shuai, J. Mao, S. Song, Q. Zhu, J. Sun, Y. Wang, R. He, J. Zhou, G. Chen, D. J. Singh, Z. Ren, *Energy Environ. Sci.* **2017**, *10*, 799.
- [76] S. Kasap, C. Koughia, H. E. Ruda, in *Springer Handb. Electron. Photonic Mater.* (Eds: S. Kasap, P. Capper), Springer International Publishing, Cham, Switzerland **2017**, p. 1.
- [77] F. Tran, P. Blaha, K. Schwarz, *J. Phys. Condens. Matter* **2007**, *19*, 196208.
- [78] H. J. Goldsmid, J. W. Sharp, *J. Electron. Mater.* **1999**, *28*, 869.
- [79] R. Al Rahal Al Orabi, J. Hwang, C.-C. Lin, R. Gautier, B. Fontaine, W. Kim, J.-S. Rhyee, D. Wee, M. Fornari, *Chem. Mater.* **2017**, *29*, 612.

- [80] L. Wu, X. Li, S. Wang, T. Zhang, J. Yang, W. Zhang, L. Chen, J. Yang, *NPG Asia Mater.* **2017**, *9*, e343.
- [81] D. Zou, Y. Liu, S. Xie, J. Lin, H. Zheng, J. Li, *RSC Adv.* **2014**, *4*, 54819.
- [82] X. Zhang, Y. Wang, Y. Yan, C. Wang, G. Zhang, Z. Cheng, F. Ren, H. Deng, J. Zhang, *Sci. Rep.* **2016**, *6*, 33120.
- [83] J. Q. Li, S. Huang, Z. P. Chen, Y. Li, S. H. Song, F. S. Liu, W. Q. Ao, *Phys. Chem. Chem. Phys.* **2017**, *19*, 28749.
- [84] K. Mori, H. Usui, H. Sakakibara, K. Kuroki, *AIP Adv.* **2012**, *2*, 042108.
- [85] I. R. Panneerselvam, C. Baldo, M. Sahasranaman, S. Murugesan, N. Rangaswamy, S. Devi Kalathiparambil Rajendra Pai, Y. Selvarathinam, *ACS Appl. Energy Mater.* **2020**, *3*, 11193.
- [86] S. Acharya, S. Anwar, T. Mori, A. Soni, *J. Mater. Chem. C* **2018**, *6*, 6489.
- [87] J.-B. Vaney, S. Aminorroaya Yamini, H. Takaki, K. Kobayashi, N. Kobayashi, T. Mori, *Mater. Today Phys.* **2019**, *9*, 100090.
- [88] F. Ahmed, N. Tsujii, T. Mori, *J. Mater. Chem. A* **2017**, *5*, 7545.
- [89] T. Mori, *Small* **2017**, *13*, 1702013.
- [90] A. Banik, T. Ghosh, R. Arora, M. Dutta, J. Pandey, S. Acharya, A. Soni, U. V. Waghmare, K. Biswas, *Energy Environ. Sci.* **2019**, *12*, 589.
- [91] M. P. Mathur, D. W. Deis, C. K. Jones, A. Patterson, W. J. C. Jr., R. C. Miller, *J. Appl. Phys.* **2003**, *41*, 1005.
- [92] S. Sugai, K. Murase, H. Kawamura, *Solid State Commun.* **1977**, *23*, 127.
- [93] G. Xie, Z. Li, T. Luo, H. Bai, J. Sun, Y. Xiao, L.-D. Zhao, J. Wu, G. Tan, X. Tang, *Nano Energy* **2020**, *69*, 104395.
- [94] G. Tan, S. Hao, R. C. Hanus, X. Zhang, S. Anand, T. P. Bailey, A. J. E. Rettie, X. Su, C. Uher, V. P. Dravid, G. J. Snyder, C. Wolverton, M. G. Kanatzidis, *ACS Energy Lett.* **2018**, *3*, 705.
- [95] M. Kaviany, *Heat Transfer Physics*, Cambridge University Press, Cambridge **2014**.
- [96] H. Wang, A. D. LaLonde, Y. Pei, G. J. Snyder, *Adv. Funct. Mater.* **2013**, *23*, 1586.
- [97] E. S. Toberer, A. Zevalkink, G. J. Snyder, *J. Mater. Chem.* **2011**, *21*, 15843.
- [98] P. M. Anderson, J. P. Hirth, J. Lothe, *Theory of Dislocations*, Cambridge University Press, Cambridge **2017**.
- [99] O. L. Anderson, *J. Phys. Chem. Solids* **1963**, *24*, 909.
- [100] W. G. Zeier, *Curr. Opin. Green Sustainable Chem.* **2017**, *4*, 23.
- [101] W. Peng, G. Petretto, G.-M. Rignanese, G. Hautier, A. Zevalkink, *Joule* **2018**, *2*, 1879.
- [102] W. Peng, D. M. Smiadak, M. G. Boehlert, S. Mather, J. B. Williams, D. T. Morelli, A. Zevalkink, *J. Appl. Phys.* **2019**, *126*, 055106.
- [103] B. Klobes, J. de Boor, A. Alatas, M. Y. Hu, R. E. Simon, R. P. Hermann, *Phys. Rev. Mater.* **2019**, *3*, 025404.
- [104] G. K. Williamson, W. H. Hall, *Acta Metall.* **1953**, *1*, 22.
- [105] T. Ungár, *Scr. Mater.* **2004**, *51*, 777.
- [106] K. Brugger, *Phys. Rev.* **1965**, *137*, A1826.
- [107] Y. Wu, Z. Chen, P. Nan, F. Xiong, S. Lin, X. Zhang, Y. Chen, L. Chen, B. Ge, Y. Pei, *Joule* **2019**, *3*, 1276.
- [108] N. F. Hinsche, I. Mertig, P. Zahn, *J. Phys. Condens. Matter* **2011**, *23*, 295502.
- [109] N. F. Hinsche, B. Yu. Yavorsky, I. Mertig, P. Zahn, *Phys. Rev. B* **2011**, *84*, 165214.
- [110] P. M. Kibasomba, S. Dhlamini, M. Maaza, C.-P. Liu, M. M. Rashad, D. A. Rayan, B. W. Mwakikunga, *Results Phys.* **2018**, *9*, 628.
- [111] M. S. Khoshkhoo, S. Scudino, J. Thomas, K. B. Surreddi, J. Eckert, *J. Alloys Compd.* **2011**, *509*, S343.
- [112] B. Srinivasan, C. Boussard-Pledel, B. Bureau, *Mater. Lett.* **2018**, *230*, 191.
- [113] Y. Pei, L. Zheng, W. Li, S. Lin, Z. Chen, Y. Wang, X. Xu, H. Yu, Y. Chen, B. Ge, *Adv. Electron. Mater.* **2016**, *2*, 1600019.
- [114] A. Banik, K. Biswas, *J. Mater. Chem. A* **2014**, *2*, 9620.
- [115] L.-D. Zhao, S.-H. Lo, Y. Zhang, H. Sun, G. Tan, C. Uher, C. Wolverton, V. P. Dravid, M. G. Kanatzidis, *Nature* **2014**, *508*, 373.
- [116] L. Lutterotti, R. Vasin, H.-R. Wenk, *Powder Diffr.* **2014**, *29*, 76.
- [117] P. Thompson, D. E. Cox, J. B. Hastings, *J. Appl. Crystallogr.* **1987**, *20*, 79.
- [118] H.-S. Kim, Z. M. Gibbs, Y. Tang, H. Wang, G. J. Snyder, *APL Mater.* **2015**, *3*, 041506.
- [119] B. Srinivasan, R. Gautier, F. Gucci, B. Fontaine, J.-F. Halet, F. Cheviré, C. Boussard-Pledel, M. J. Reece, B. Bureau, *J. Phys. Chem. C* **2018**, *122*, 227.
- [120] B. Srinivasan, C. Boussard-Pledel, V. Dorcet, M. Samanta, K. Biswas, R. Lefèvre, F. Gascoin, F. Cheviré, S. Tricot, M. Reece, B. Bureau, *Materials* **2017**, *10*, 328.
- [121] J. Simon, G. Guélou, B. Srinivasan, D. Berthebaud, T. Mori, A. Maignan, *J. Alloys Compd.* **2020**, *819*, 152999.
- [122] B. Srinivasan, D. Berthebaud, T. Mori, *Energies* **2020**, *13*, 643.
- [123] P. Blaha, K. Schwarz, G. Madsen, D. Kvasnicka, J. Luitz, *WIEN2K: An Augmented Plane Wave plus Local Orbitals Program for Calculating Crystal Properties*, Vienna University of Technology, Vienna **2001**.
- [124] J. P. Perdew, K. Burke, M. Ernzerhof, *Phys. Rev. Lett.* **1996**, *77*, 3865.
- [125] J. P. Perdew, A. Ruzsinszky, G. I. Csonka, O. A. Vydrov, G. E. Scuseria, L. A. Constantin, X. Zhou, K. Burke, *Phys. Rev. Lett.* **2008**, *100*, 136406.